nature chemical biology

Article

https://doi.org/10.1038/s41589-022-01166-5

Structural basis of TRPV3 inhibition by an antagonist

Received: 7 January 2022

Accepted: 8 September 2022

Junping Fan[1,6], Linghan Hu[2,6], Zongwei Yue[1,6], Daohong Liao[3,6], Fusheng Guo[1], Han Ke[1], Daohua Jiang[4,5,7] ✉, Yong Yang[2,7] ✉ and Xiaoguang Lei[1,7] ✉

The TRPV3 channel plays vital roles in skin physiology. Dysfunction of TRPV3 causes skin diseases, including Olmsted syndrome. However, the lack of potent and selective inhibitors impedes the validation of TRPV3 as a therapeutic target. In this study, we identified Trpvicin as a potent and subtype-selective inhibitor of TRPV3. Trpvicin exhibits pharmacological potential in the inhibition of itch and hair loss in mouse models. Cryogenic electron microscopy structures of TRPV3 and the pathogenic G573S mutant complexed with Trpvicin reveal detailed ligand-binding sites, suggesting that Trpvicin inhibits the TRPV3 channel by stabilizing it in a closed state. Our G573S mutant structures demonstrate that the mutation causes a dilated pore, generating constitutive opening activity. Trpvicin accesses additional binding sites inside the central cavity of the G573S mutant to remodel the channel symmetry and block the channel. Together, our results provide mechanistic insights into the inhibition of TRPV3 by Trpvicin and support TRPV3-related drug development.

As a symptom commonly associated with various forms of dermatitis, such as senile xerosis and atopic dermatitis (AD), chronic itching or pruritus affects millions of people worldwide[1,2]. Histamine H1 receptor antagonists have been routinely used as anti-pruritic therapy but are often ineffective against many types of itch[3]. Therefore, there is an unmet need for new therapeutics in itch treatment. Currently, transient receptor potential (TRP) channels are on center stage, with growing evidence suggesting their key roles in pain and itch perception[2,4–6]. TRP channels are a family of non-selective cation channels that serve as sensors for various physical and chemical stimuli[7–9]. Among them, the vanilloid TRP (TRPV) subfamily is composed of six members (TRPV1–TRPV6), four of which (TRPV1–TRPV4) are activated by heat[10,11]. TRPV3 is a calcium-permeable non-selective cation channel that responds to moderate temperature (~33 °C) and chemical stimuli, such as synthetic small molecules (for example, 2-aminoethoxydiphenyl borate (2-APB)) and many natural compounds (for example, camphor)[12–14]. TRPV3 is predominantly expressed in epidermal and hair follicle keratinocytes and plays important roles in many aspects of skin functions[15–19]. In particular, our previous findings demonstrated that a series of pathogenic mutations of TRPV3, including G573S, G573C, W692G and G568V, are linked to Olmsted syndrome (OS)[20,21]. Furthermore, our recent investigations have shown that TRPV3 is associated with other skin diseases, such as AD[22]. In contrast to other thermo-TRP channels, TRPV3 becomes sensitized rather than desensitized after repetitive stimulation[23], which suggests that TRPV3 must be inhibited to alleviate TRPV3-related diseases. Consequently, the identification of potent small molecules targeting TRPV3 may provide therapeutic benefits in the treatment of related diseases.

---

[1]Beijing National Laboratory for Molecular Sciences, Key Laboratory of Bioorganic Chemistry and Molecular Engineering of Ministry of Education, Department of Chemical Biology, College of Chemistry and Molecular Engineering, Synthetic and Functional Biomolecules Center and Peking-Tsinghua Center for Life Sciences, Peking University, Beijing, China. [2]Jiangsu Key Laboratory of Molecular Biology for Skin Diseases and STIs, Institute of Dermatology, Chinese Academy of Medical Sciences and Peking Union Medical College, Nanjing, China. [3]Iongen Therapeutics Co. Ltd., Nanjing, China. [4]Laboratory of Soft Matter Physics, Institute of Physics, Chinese Academy of Sciences, Beijing, China. [5]University of Chinese Academy of Sciences, Beijing, China. [6]These authors contributed equally: Junping Fan, Linghan Hu, Zongwei Yue, Daohong Liao. [7]These authors jointly supervised this work: Daohua Jiang, Yong Yang, Xiaoguang Lei. ✉e-mail: jiangdh@iphy.ac.cn; yyang@pumcderm.cams.cn; xglei@pku.edu.cn

Recently reported cryogenic electron microscopy (cryo-EM) structures of TRPV3 revealed the molecular mechanisms underlying the sensitization and gating modulation by heat, agonists or lipids[24–28]. The structures of TRPV3 in detergent micelles suggested that the pore-lining S6 helices underwent α- to π-helix transitions during sensitization. Interestingly, the structures of TRPV3 in lipid nanodiscs revealed that lipid binding could stabilize both the selectivity filter (SF) and the intracellular gate in a closed state, despite the S6 helix still adopting the π-helical configuration[29,30]. These results suggest a complicated activation mechanism of TRPV3 in the natural lipid environment and suggest that the sensitization of TRPV3 is finely tuned by lipids or chemical stimuli. Nevertheless, the mechanism by which TRPV3 is inhibited by a potent antagonist remains unclear. Meanwhile, the lack of detailed structural information for the antagonist-binding site hinders the rational design of selective and potent inhibitors for TRPV3.

In this study, we identified the compound N-(5-(2-(2-cyanopropan-2-yl)pyridin-4-yl)-4-(trifluoromethyl)thiazol-2-yl)-4,6-dimethoxypyrimidine-5-carboxamide (Trpvicin, **1**) as a potent and subtype-selective antagonist of TRPV3. We also demonstrated the effectiveness of Trpvicin in multiple mouse models. We further determined the cryo-EM structures of the TRPV3–Trpvicin complex and mapped detailed binding pockets for this antagonist, elucidating the inhibition mechanism for Trpvicin. Additionally, the structures of the G573S mutant provided mechanistic insights into how the pathogenic mutation causes the overactivation of TRPV3. Trpvicin can also inhibit the G573S mutant by accessing additional binding sites in the central cavity through the enlarged activation gate or fenestrations.

Results

Trpvicin inhibits TRPV3

Taking advantage of the pathogenic mutant of human TRPV3 G573S (hTRPV3-G573S) causing cytotoxicity[21], we established a high-throughput screening platform to search for potential small molecules that can block the constant leak current and reverse the cytotoxicity (Fig. 1a). Through screening an in-house chemical library (~110,000 compounds) containing natural products, FDA-approved drugs and a number of literature-reported or patent-reported small-molecule inhibitors for TRPV channels[31–33], we found that Trpvicin[34] (Supplementary Note 1) showed promising efficacy in blocking cytotoxicity (Fig. 1b,c). We then carried out electrophysiological studies on human TRPV3 wild-type (hTRPV3-WT) and hTRPV3-G573S transiently expressed in HEK293T cells. Compared to the hTRPV3-WT channel, which generates currents with the stimulation of 2-APB, hTRPV3-G573S produces pronounced leak currents even without 2-APB (Fig. 1d,e). Notably, Trpvicin exhibits promising efficacy in antagonizing both hTRPV3-WT and hTRPV3-G573S channels. Increasing Trpvicin concentrations (1 nM–100 μM) caused a gradual current reduction of the hTRPV3-WT channel elicited by 300 μM 2-APB (Fig. 1d). Meanwhile, Trpvicin exhibited a similar dose-dependent inhibition of the leak current of hTRPV3-G573S (Fig. 1e). Trpvicin at 10 μM or higher almost completely inhibited the currents, which is comparable to the inhibitory effect of 10 μM ruthenium red (RR), a broad-spectrum TRP channel blocker[35] (Fig. 1e). The half-maximum inhibitory concentration (IC_{50}) values for hTRPV3-WT and hTRPV3-G573S were 0.41 μM and 0.22 μM, respectively (Fig. 1g). To assess the potential selectivity of Trpvicin, two independent repetitions of in vitro pharmacological profiling were conducted. The interference of native ligand binding of a total of 47 targets, including receptors, ion channels, enzymes and transporters, by 10 μM Trpvicin was evaluated. The results showed that the inhibition (or stimulation) was all below 40% except PDE4D2, which was inhibited by nearly 70% (Supplementary Table 1), indicating that Trpvicin has a non-substantial or weak effect on the tested targets. Regarding the subtype selectivity of Trpvicin, we evaluated its inhibitory effect on TRPV1–6 channels heterologously expressed in HEK293T cells. Strikingly, Trpvicin displayed remarkable selectivity for TRPV3 over all other tested TRPV channels (Fig. 1h,i and Extended Data Fig. 1a–e). In addition, Trpvicin showed much weaker, if any, inhibitory effects on other tested TRP family members, such as TRPA1 and TRPM8 (Extended Data Fig. 1f–i). These results strongly suggest that Trpvicin is a potent and subtype-selective inhibitor of TRPV3.

Relief of itch and hair loss in mouse models with Trpvicin

Our previous studies suggested that knockout of TRPV3 can reduce the scratching behavior of mice in both acute itch elicited by the protease-activated receptor 2 (PAR2) agonist SLIGRL and chronic itch in an AD-like model induced by calcipotriol (MC903), a vitamin D3 analog[22,36]. To assess the effect of Trpvicin on mouse models, we first confirmed that Trpvicin can potently inhibit mouse TRPV3 (mTRPV3) with an IC_{50} of 0.38 μM (Extended Data Fig. 2a,b). We then tested different concentrations of Trpvicin in both the acute and chronic itch mouse models based on the pharmacokinetic parameters of Trpvicin (Supplementary Table 2). WT mice were intradermally injected with SLIGRL and vehicle, and mice concurrently treated with 10 μM or 100 μM Trpvicin exhibited fewer scratching bouts elicited by SLIGRL (Extended Data Fig. 2c). Similarly, for chronic itch, compared to control mice gavaged with vehicle only, the scratching behavior of WT mice topically treated with MC903 was reduced when concurrently gavaged with 100 mg kg^{-1} of Trpvicin (Extended Data Fig. 2d). Moreover, the percentage of ear thickness increase induced by MC903 was also reduced in the Trpvicin-treated groups (Extended Data Fig. 2e).

Recently, we generated a *Trpv3* knock-in mouse model with the gain-of-function mutation G568V. The resulting heterozygous *Trpv3*$^{+/G568V}$ knock-in mice showed symptoms similar to those of patients with OS, especially hair loss[37]. Similarly to hTRPV3-G573S (Supplementary Fig. 1a,b), we found that 10–100 μM Trpvicin inhibited the currents of hTRPV3-G568V and mTRPV3-G568V heterologously expressed in HEK293T cells (Extended Data Fig. 2a,b and Supplementary Fig. 1c). We also transfected HEK293T cells with mTRPV3 WT and G568V at a 1:1 ratio to mimic the condition of the heterozygous *Trpv3*$^{+/G568V}$ mice and found that the IC_{50} was in between (Extended Data Fig. 2b). To investigate the effect of Trpvicin on the *Trpv3*$^{+/G568V}$ mouse model, we topically treated mice on their backs once per day with a homemade cream containing 1 wt% Trpvicin starting from postnatal day 50 (P50). In contrast to the vehicle-treated control mice with alternating hair growth and loss, *Trpv3*$^{+/G568V}$ mice treated with 1 wt% Trpvicin showed substantially longer hair shafts and less hair shedding throughout the period of treatment (Extended Data Fig. 2f,g and Supplementary Fig. 1d). In addition, the rescue of hair loss by Trpvicin treatment occurred in both male and female mouse models. Taken together, these results suggest that Trpvicin may serve as a hit compound for the potential development of drugs for TRPV3-associated diseases.

Cryo-EM structure reveals a detailed Trpvicin-binding site

To unveil the molecular mechanism underlying the inhibition of TRPV3 by Trpvicin, we sought to solve the cryo-EM structure of TRPV3 in complex with Trpvicin. The full-length hTRPV3-WT protein was expressed in HEK293F cells[38], and the homogeneous sample was purified in detergent micelles (Supplementary Fig. 2a). To obtain the antagonist–channel complex, Trpvicin was added throughout the expression and purification processes. We performed cryo-EM single-particle analysis of the purified hTRPV3 samples and refined the C4 symmetry-imposed reconstruction maps of apo form hTRPV3 ($hTRPV3_{apo}$) and Trpvicin-bound hTRPV3 ($hTRPV3_{Trpvicin}$) to 3.5 Å and 2.5 Å, respectively (Extended Data Fig. 3). The higher resolution of the $hTRPV3_{Trpvicin}$ complex is likely due to the stabilization of the channel upon Trpvicin binding, supported by the lower B-factor distribution in the TM-core of $hTRPV3_{Trpvicin}$ than that of $hTRPV3_{apo}$ (Extended Data Fig. 4a,b). The excellent density map allowed us to build accurate models for TRPV3 and ligands (Fig. 2a). The overall structure of hTRPV3 resembles the structures of hTRPV3 or

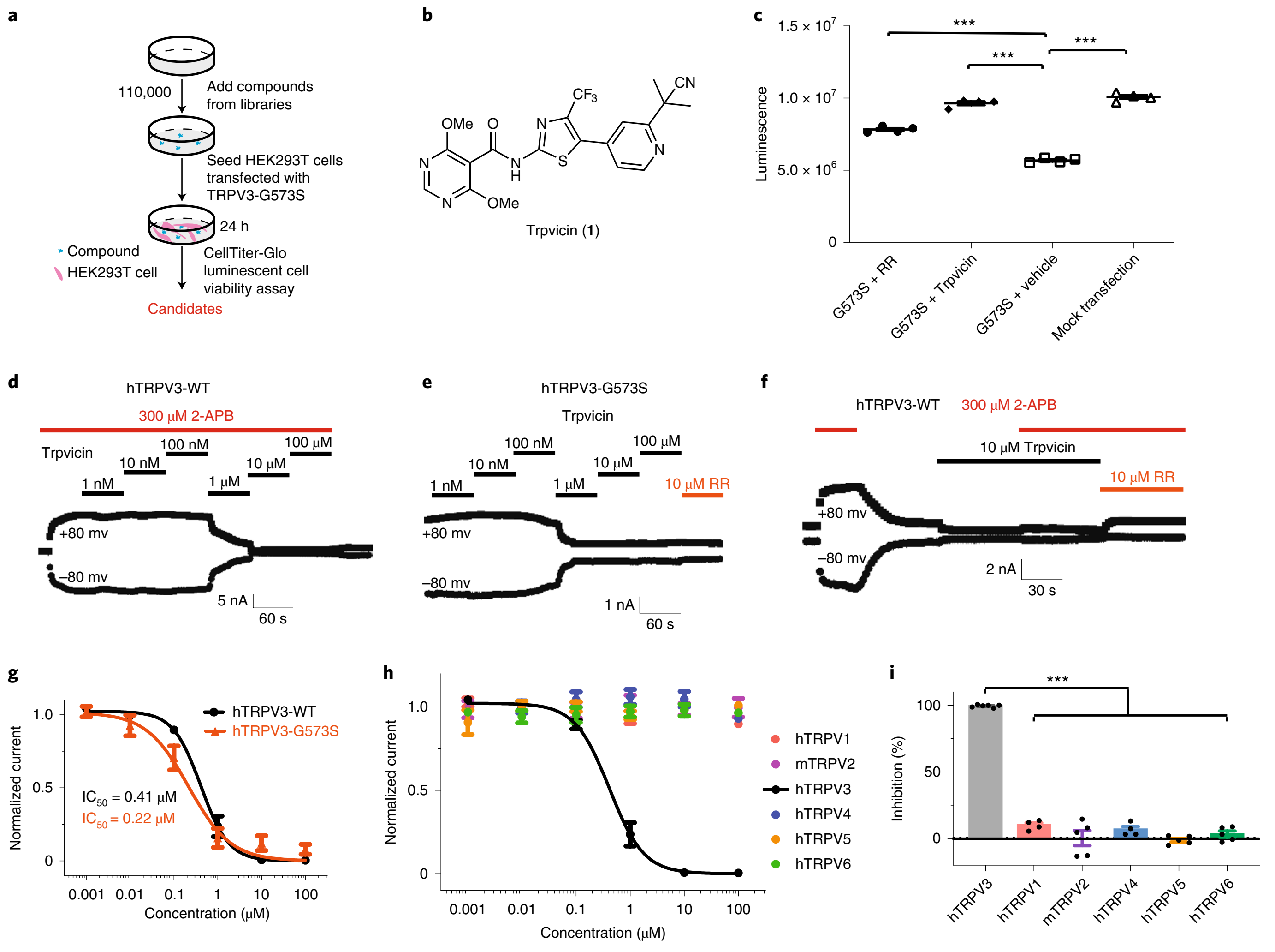

Fig. 1 | Trpvicin inhibits TRPV3. a, Schematic diagram of high-throughput screening based on cell toxicity of the hTRPV3-G573S mutant. **b**, Chemical structure of Trpvicin. **c**, Comparison of cell viability of hTRPV3-G573S-transfected HEK293T cells treated with 10 μM RR, 10 μM Trpvicin or vehicle, together with mock-transfected cells. One-way ANOVA ($P = 1.64 \times 10^{-11}$) followed by Bonferroni post tests, $n = 4$. Data are presented as mean values ± s.e.m. RR, ruthenium red. **d**, The representative current traces of hTRPV3-WT TRPV3 in response to 2-APB (300 μM, red bar) and co-application of increasing concentrations of Trpvicin (from 1 nM to 100 μM, black bar), at ±80 mV. **e**, The representative current traces of hTRPV3-G573S inhibited by increasing concentrations of Trpvicin (from 1 nM to 100 μM, black bar), at ±80 mV. 10 μM RR was used to assess the whole amplitudes of the leak current. **f**, The representative current traces of hTRPV3-WT in response to 2-APB (300 μM, red bar) or Trpvicin (10 μM, black bar) alone, followed by co-application of both compounds at ±80 mV. **g**, Curve fitting of dose-dependent inhibition of 300 μM 2-APB-evoked hTRPV3-WT current or hTRPV3-G573S leak current at −80 mV by Trpvicin (hTRPV3-WT, log-$IC_{50} = -0.38 \pm 0.06$, $n = 6$ biologically independent cells; hTRPV3-G573S, log-$IC_{50} = -0.66 \pm 0.13$, $n = 5$ biologically independent cells). Data are presented as mean values ± s.e.m. **h**,**i**, Dose–response analysis of the different concentrations of Trpvicin (**h**) and summary of the percent of inhibition by 100 μM Trpvicin (**i**) on agonist-evoked currents of hTRPV1 (1 μM capsaicin, at +80 mV, $n = 4$), mTRPV2 (1 mM probenecid, at +80 mV, $n = 5$) and hTRPV4 (100 nM GSK1016790A, at −80 mV, $n = 4$), together with inherent currents at −80 mV of hTRPV5 and hTRPV6 (both $n = 5$), compared to hTRPV3 (300 μM 2-APB, at −80 mV, $n = 6$). One-way ANOVA ($P = 8.36 \times 10^{-19}$) followed by Bonferroni post tests. Data are presented as mean values ± s.e.m.; $^{***}P < 0.001$. Same data sets of hTRPV3-WT were used for Fig. 1g,h.

mTRPV3 in lipid nanodiscs[29,30] (Extended Data Fig. 5a,b). Notably, four pieces of unambiguous density, which are absent in our hTRPV3$_{apo}$ map, are located between the voltage-sensor-like domain (VSLD) of each subunit and the pore domain (PD) of the adjacent subunit (Fig. 2b,c). Trpvicin fits perfectly inside this density, revealing a ligand-binding site. Trpvicin wedges in the cleft formed by transmembrane segment 4 (S4) of each VSLD and S5–S6 from the adjacent PD. The binding of Trpvicin is stabilized by extensive hydrophobic interactions and van der Waals contacts, as well as hydrogen bonds, based on the high-resolution map density[39] (Fig. 2b,c). The short sidechain residues A556 and A560 play key roles in making space in the cleft to accommodate the head of Trpvicin (Fig. 2c); the bulky residues W559, F597 and F601 sandwich the dimethoxypyrimidine group of Trpvicin; and T660 and I663 contribute to stabilizing the pyridine and gem-dimethyl groups (Fig. 2b,c). To evaluate the specific interactions between hTRPV3 and Trpvicin, we examined the effect of Trpvicin on a series of point-mutated hTRPV3 variants based on sequences of the TRPV subfamily and alanine scanning. Only mutants that functioned similarly to hTRPV3-WT in response to 300 μM 2-APB were chosen for further investigation (Extended Data Fig. 6a,e). Compared to hTRPV3-WT, the mutations A556V, A560T and F601A substantially decreased the potency of Trpvicin by 158-fold, 162-fold and 208-fold, respectively (Fig. 2d and Extended Data Fig. 6a), suggesting that these residues are the key determinants for Trpvicin binding. Meanwhile, T660A decreased the potency of Trpvicin by only 2.4-fold (Fig. 2d and Extended Data Fig. 6a), indicating that this residue is less important for Trpvicin binding. For F597, mutations including

https://doi.org/10.1038/s41589-022-01166-5

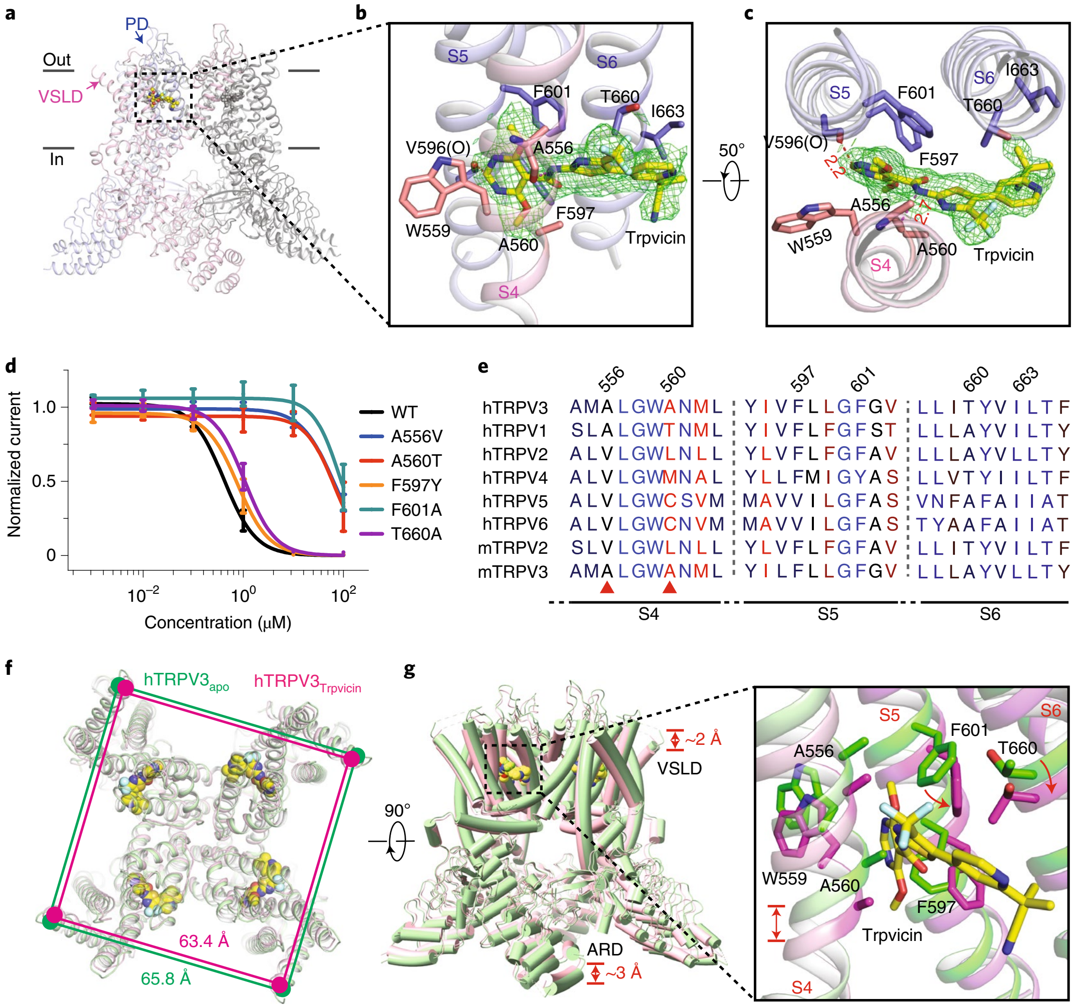

Fig. 2 | The detailed VSLD-PD-binding site for Trpvicin in TRPV3. **a**, Overall structure of $hTRPV3_{Trpvicin}$ viewed parallel to the membrane. **b**,**c**, Close-up views for the detailed interactions between hTRPV3 and Trpvicin from the side (**b**) and top-down (**c**), respectively. Trpvicin is shown in sticks and colored with carbon atoms in yellow, oxygen in red, fluorine in cyan and nitrogen in blue. The density for Trpvicin is contoured at 5σ (green mesh). The S4 and S5–S6 from the adjacent subunit are colored in light pink and light blue, respectively. Sidechains of key residues interacting with Trpvicin are shown in sticks. Hydron bonds are indicated with red dashed lines and with distances labeled. **d**, Curve fitting of dose-dependent inhibition of 300 μM 2-APB-evoked currents at −80 mV by Trpvicin on various hTRPV3 mutants compared to WT (WT, log-IC_{50} = −0.38 ± 0.06, *n* = 6; A556V, log-IC_{50} = 1.81 ± 0.07, *n* = 4; A560T, log-IC_{50} = 1.82 ± 0.14, *n* = 4; F597Y, log-IC_{50} = −0.11 ± 0.09, *n* = 4; F601A, log-IC_{50} = 1.93 ± 0.11, *n* = 4; T660A, log-IC_{50} = 0.03 ± 0.05, *n* = 5). Data are presented as mean values ± s.e.m. **e**, Sequence alignment of the human and mouse TRPV channels. The residues are colored based on sequence similarity, with high conserved in blue and less conserved in red. Residues contributed to Trpvicin binding are labeled. The red triangles indicate key residues for Trpvicin binding and selectivity. F597, F601 and T660 are also important for Trpvicin binding. **f**,**g**, Superposition of the $hTRPV3_{apo}$ structure (light green) and $hTRPV3_{Trpvicin}$ (light pink) viewed from top-down (**f**) and side (**g**), respectively. The black dashed square indicates a close-up view of the local conformational changes induced by Trpvicin binding.

F597V, F597A, F597L or F597W (bulky residues) failed to evoke detectable currents in response to 2-APB; and F597Y only slightly decreased the potency of Trpvicin by 1.8-fold (Fig. 2d and Extended Data Fig. 6a), which indicated that F597Y could also provide similar van de Waals contact with Trpvicin. To further evaluate the contribution of F597 to Trpvicin binding, the MM/GBSA binding affinity calculations were conducted, and the results showed that F597 contributes to Trpvicin binding as much as A560 (Extended Data Fig. 6d). Interestingly, among these key residues for Trpvicin binding, A560 is not conserved among hTRPV1-6; A556 is less conserved, at the corresponding position an Ala residue only appearing in TRPV1 but not other TRPV channels; and F597 and F601 are relatively conserved (Fig. 2e). Therefore, we postulate that the subtype-selective inhibition of Trpvicin on hTRPV3 is mainly determined by A556 and A560. This pocket in other TRPV channels does not enable Trpvicin binding, thus conferring Trpvicin subtype selectivity.

$hTRPV3_{apo}$ and $hTRPV3_{Trpvicin}$ share a similar overall structure with a root mean square deviation (RMSD) of 1.68 Å. However, the $hTRPV3_{Trpvicin}$ structure appears to be shrunken by ~2.4 Å and ~5.0 Å in the directions parallel and perpendicular to the membrane plane, respectively (Fig. 2f,g). A closer look shows that Trpvicin binding induces marked local conformational changes, such as sidechain rotations of F597, F601 and T660 (Fig. 2g). We also observed a more constricted ion path of 4.6 Å at the SF and 5.6 Å at the activation gate (Fig. 4a), which are smaller than that of the closed-state $hTRPV3_{apo}$. These structural observations suggest that Trpvicin binding stabilizes hTRPV3 in a more closed state, elucidating the molecular mechanism of TRPV3 inhibition by Trpvicin. Trpvicin binds in the VSLD-PD pocket of TRPV3 and traps the channel in a more closed conformation, preventing the channel from opening. To validate this hypothesis, we treated hTRPV3-expressing HEK293T cells with 10 μM Trpvicin for 1 minute before applying 2-APB

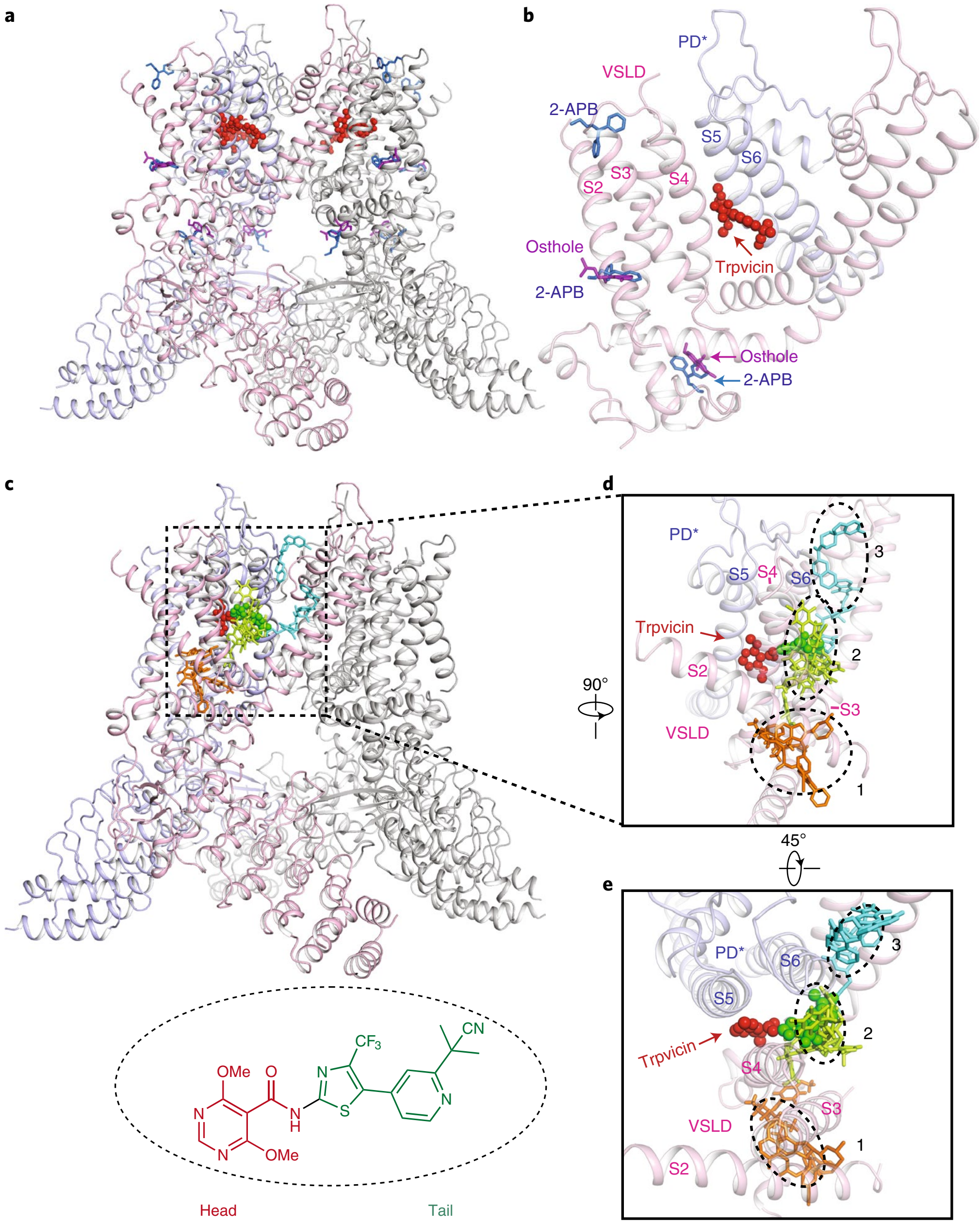

Fig. 3 | Trpvicin binds to a VSLD-PD pocket. a, Ligand-binding sites in TRPV3. Overlay of the ligand-bound structures of TRPV3 of the mTRPV3-Y564A$_{\text{osthole}}$ (PDB code: 7RAS) and mTRPV3-Y564A$_{\text{2-APB}}$ (PDB code: 6DVZ) with hTRPV3$_{\text{Trpvicin}}$. Trpvicin shown as spheres and Osthole and 2-APB shown as sticks are colored in red, purple and marine, respectively. **b**, The transmembrane domain and the TRP helix of TRPV3 from one subunit are presented for clarity. **c**, Ligand-binding sites in TRP channels. Representation of reported TRP channels ligand-binding sites in VSLD (site 1), vanilloid (site 2) and pore region (site 3) binding pockets shown on TRPV3. Ligands located in the pockets are shown as sticks and colored in orange, limon and cyan for sites 1–3, respectively. The PDBs shown here include RTX in TRPV1 (PDB code: 5IRX), ECN in TRPV5 (PDB code: 6B5V) and GNE551 in TRPA1 (PDB code: 6X2J) bound to the vanilloid pocket; WS-12 in TRPM8 (PDB code: 6NR2), AM-1473 in TRPC6 (PDB code: 6UZA) and ZINC17988990 in TRPV5 (PDB code: 6PBE) bound to the VSLD domain; and CBD in TRPV2 (PDB code: 6U88), ML-SA1 in TRPML1 (PDB code: 5WJ9) and AM0883 in TRPC6 (PDB code: 6UZ8) bound to the pore region binding pocket. Trpvicin's structure is shown with head (red) and tail (green) named. **d**,**e**, Close-up views for the binding pockets of TRP channel from the side (**d**) and top-down (**e**) view, respectively. The Trpvicin is shown in spheres with the same color scheme as in **c** and indicated by a red arrow.

and found that almost no current was evoked by 2-APB (Fig. 1f), which strongly suggests that Trpvicin traps hTRPV3 in the closed state.

Trpvicin inhibits hTRPV3 by binding to the VSLD-PD site, as revealed by our cryo-EM structure. Distinct from known ligand-binding sites in TRPV3 (ref. [31]), which are located in the VSLD or close to the TRP helix (Fig. 3a,b), the Trpvicin binding site is located between the VSLD and adjacent PD in the middle of the lipid bilayer. Lipophilic Trpvicin can quickly integrate into the membrane and access the binding site. Moreover, this binding site is at least partially different from currently known TRP channel ligand-binding sites[40], which are classified as site 1 (in VSLD), site 2 (vanilloid) and site 3 (pore region). Trpvicin can be divided into two parts, with the dimethoxypyrimidine and amid part as the head and the rest as the tail (Fig. 3c). The tail part partially overlaps with the previous ligands that bind in the vanilloid pocket, whereas the head part binds to the pocket in the VSLD-PD site (Fig. 3c–e). The main interactions that determine the recognition and selectivity of

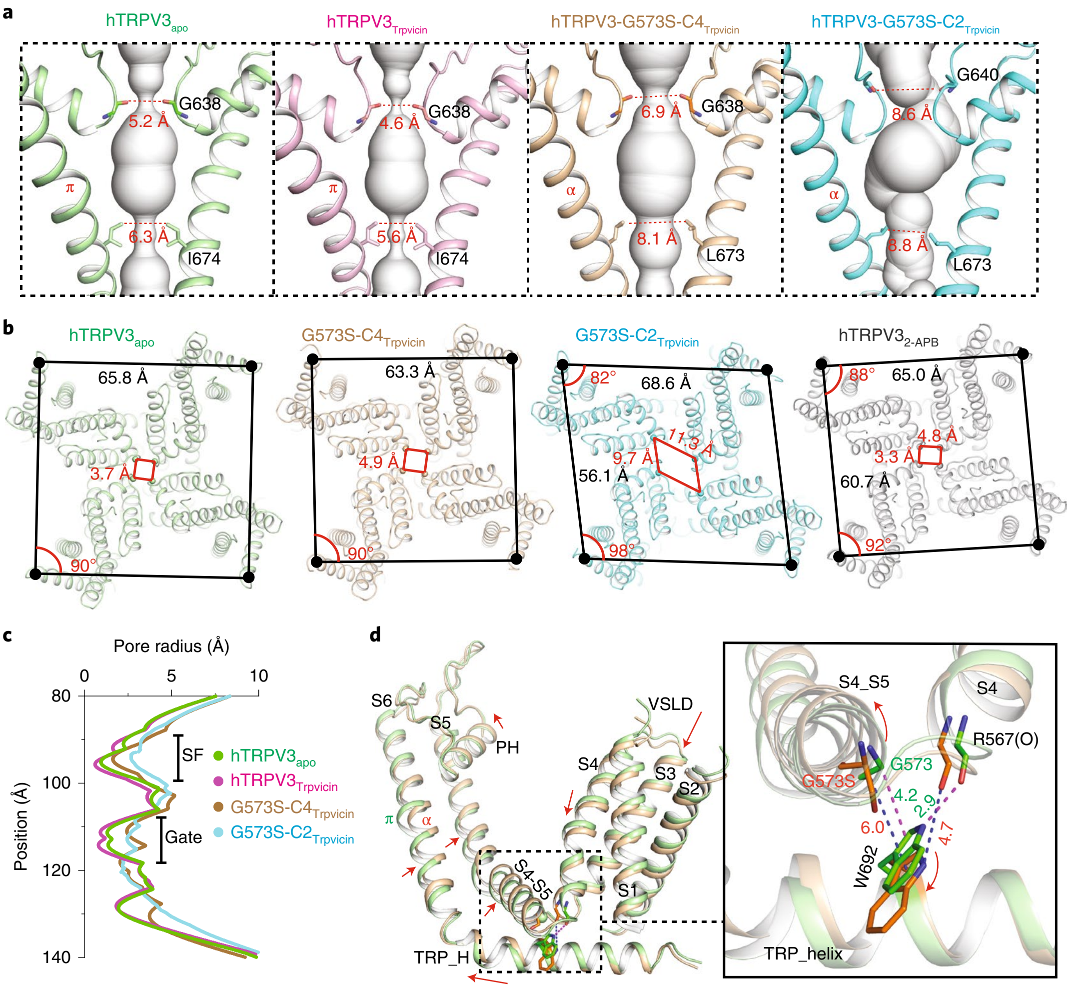

Fig. 4 | G573S mutation expands the ion path of hTRPV3. a, The ion-conduction pores of hTRPV3 structures are shown as white spheres, calculated with HOLE. Only two opposing subunits of pore domains are shown for clarity; diagonal distances at the two narrowest constriction points are labeled and shown with dashed lines. **b**, Structural rearrangements of the hTRPV3-G573S structures. The C4 symmetric hTRPV3-G573S-$C4_{Trpvicin}$ structure (wheat) shows enlarged SF compared to the $hTRPV3_{apo}$ (pale green), and the C2 symmetric hTRPV3-G573S-$C2_{Trpvicin}$ (cyan) is apparent different compared to the $hTRPV3_{2\text{-}APB}$ (PDB code: 6MHW) in C2 symmetry (gray). The black dots indicate the size and shape of the transmembrane domain of each structure. The glycine residues at the constriction sites of the SF shown as spheres indicate the conformational changes of the SF in each structure. **c**, The pore radius along the permeation pathway was calculated with the HOLE of the four structures. Two constriction sites of the SF and the activation gate are shown as SF and Gate. **d**, Superposition of the VSLD and PD from $hTRPV3_{apo}$ (pale green) and hTRPV3-G573S-$C4_{Trpvicin}$ (wheat). The red arrows indicate the conformational shifts induced by the hTRPV3-G573S mutation. On the right shows the close-up view of the dashed square in the aligned subunit.

Trpvicin come from its head (red), which wedges in the cleft of VSLD and pore domain, and these key interactions are distinct from the non-selective vanilloid site (site 2), so this site can be considered as a vanilloid extended pocket. The Trpvicin-binding site not only confers Trpvicin subtype selectivity but also provides a structural template for further rational drug design.

G573S mutation expands the ion path of TRPV3

To understand the molecular mechanisms underlying the constitutive opening and inhibition of the pathogenic mutant by Trpvicin, we carried out cryo-EM structural studies. hTRPV3-G573S displayed a higher affinity than hTRPV3-G568V (Fig. 1g and Supplementary Fig. 1b). Therefore, we decided to study hTRPV3-G573S by cryo-EM because it should have a higher chance of obtaining the complex structure. We successfully purified the hTRPV3-G573S sample by expressing the protein in the presence of 10 μM Trpvicin to reduce the cytotoxicity (Supplementary Fig. 2b). Unexpectedly, three-dimensional (3D) analysis of the cryo-EM data without imposing symmetry generated two different maps (Extended Data Fig. 7) composed of 48,492 and 152,978 particles, respectively. The first map of the smaller class displayed apparent C4 symmetry, whereas the second map of the larger class showed obvious C2 symmetry. The two classes were finally refined with C4 and C2 symmetry to 3.6 Å and 2.9 Å, respectively (Extended Data Figs. 7 and 4c,d). The resulting two structures were termed hTRPV3-G573S-$C4_{Trpvicin}$ and hTRPV3-G573S-$C2_{Trpvicin}$. We observed substantial conformational changes in both the hTRPV3-G573S-$C4_{Trpvicin}$ and hTRPV3-G573S-$C2_{Trpvicin}$ structures, which have overall RMSD values of 1.24 Å and 3.38 Å, respectively, compared to the $hTRPV3_{apo}$ structure, suggesting that the hTRPV3-G573S-$C2_{Trpvicin}$ structure is more different from the $hTRPV3_{apo}$ structure (Fig. 4b). The symmetry transitions of the TRPV channel were thought to be involved in channel gating, which was observed in the structures of TRPV2 (ref. [41]), TRPV3 in C2 symmetry[27] and TRPV5 in C1 symmetry[42,43]. However, the diamond-shaped hTRPV3-G573S-$C2_{Trpvicin}$ manifests substantial structural differences from hTRPV3-G573S-$C4_{Trpvicin}$ or the previously reported TRPV3 structure in C2 symmetry[27] (Fig. 4b).

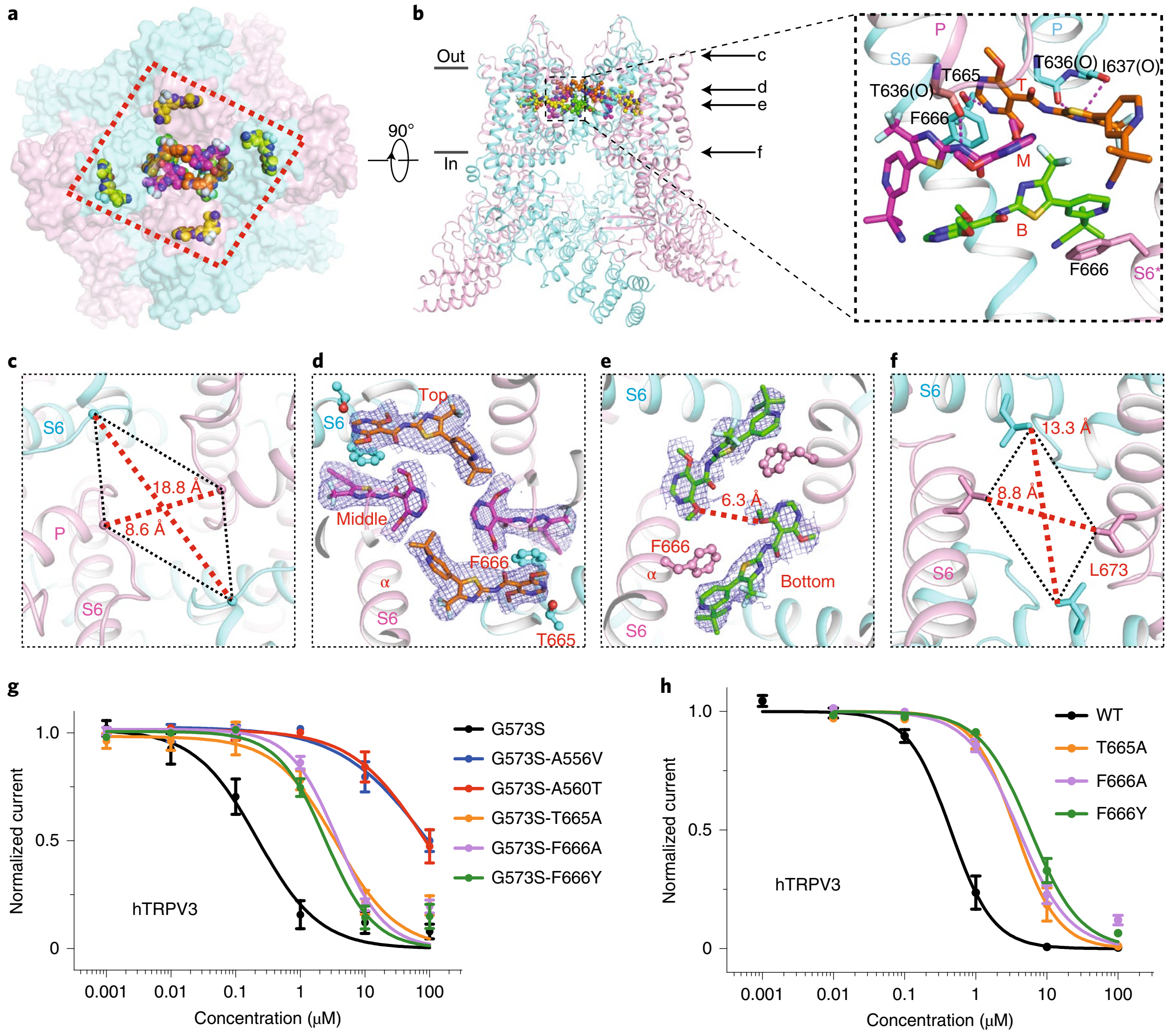

Fig. 5 | Symmetry remodeling and pore blocking of G573S-C2 by Trpvicin. **a**, Ten Trpvicin molecules bound in the hTRPV3-G573S-C2 structure, four Trpvicin molecules bound in the VSLD-PD site between VSLD and PD and six Trpvicin molecules bound in the pore binding sites in the central cavity. **b**, The overall structure of hTRPV3-G573S-C2 in complex with Trpvicin is shown in the cartoon. Trpvicin molecules are shown in spheres. On the right is a close-up view of the Trpvicin pore binding sites. Trpvicins are shown in sticks and colored orange (top layer, T), purple (middle layer, M) and green (bottom layer, B), respectively. Key residues sidechains are shown in sticks. Arrows denote positions of hTRPV3-G573S-C2$_{\text{Trpvicin}}$ for horizontal cross-sections shown in panels (**c**–**f**). **c**, Rectangle-shaped selectivity filter of hTRPV3-G573S-C2$_{\text{Trpvicin}}$. **d**,**e**, The top and middle layers (**d**) and bottom layer (**e**) of Trpvicin binding in the central cavity of hTRPV3-G573S-C2$_{\text{Trpvicin}}$ block the ion path. The sidechains of F666 and T665 interacting with Trpvicin are shown in spheres. **f**, The diamond-shaped activation gate of hTRPV3-G573S-C2$_{\text{Trpvicin}}$. **g**, Curve fitting of dose-dependent inhibition of hTRPV3 leak currents at −80 mV by Trpvicin on hTRPV3-G573S-A556, hTRPV3-G573S-A560, hTRPV3-G573S-F666 and hTRPV3-G573S-T665 mutants (hTRPV3-G573S, log-IC$_{50}$ = −0.66 ± 0.13, *n* = 5; G573S-A556V, log-IC$_{50}$ = 1.94 ± 0.11, *n* = 4, G573S-A560T, log-IC$_{50}$ = 1.92 ± 0.10, *n* = 4; G573S-T665A, log-IC$_{50}$ = 0.56 ± 0.12, *n* = 4; G573S-F666A, log-IC$_{50}$ = 0.57 ± 0.07, *n* = 5; G573S-F666Y, log-IC$_{50}$ = 0.39 ± 0.08, *n* = 4). The datasets of hTRPV3-G573S are the same as Fig. 1g. Data are presented as mean values ± s.e.m. **h**, Curve fitting of dose-dependent inhibition of 300 μM 2-APB-evoked hTRPV3 currents at −80 mV by Trpvicin on hTRPV3-F666 and hTRPV3-T665 mutants (hTRPV3-T665A, log-IC$_{50}$ = 0.56 ± 0.05, *n* = 5; hTRPV3-F666A, log-IC$_{50}$ = 0.60 ± 0.05, *n* = 5; hTRPV3-F666Y, log-IC$_{50}$ = 0.77 ± 0.04, *n* = 5). The datasets of hTRPV3-WT are the same as Fig. 1g. Data are presented as mean values ± s.e.m.

The hTRPV3-G573S-C4$_{\text{Trpvicin}}$ structure contains an ion path with a 6.9-Å SF and an 8.1-Å activation gate (Fig. 4a), which is markedly larger than that of TRPV3$_{\text{apo}}$ (Fig. 4a,c) but still smaller than the reported open-state structure of TRPV3 with a 7.2 Å SF and a 9.3 Å activation gate[24] (Extended Data Fig. 5c,d). Similarly to the hTRPV3$_{\text{Trpvicin}}$ structure, four pieces of strong density representing the Trpvicin molecules were observed at the VSLD-PD sites of hTRPV3-G573S-C4$_{\text{Trpvicin}}$ (Extended Data Figs. 8a–c and 9b). The hTRPV3-G573S mutant was considered a fully open channel because it can hardly be further activated by 2-APB[21]. The smaller ion path of Trpvicin-bound hTRPV3-G573S-C4$_{\text{Trpvicin}}$ suggests that the antagonist binding may still prevent the full opening of the mutant channel. Similarly to hTRPV3-WT, the A556V and A560T mutations of hTRPV3-G573S also decreased the potency of Trpvicin by 398-fold and 381-fold, respectively (Fig. 5g and Extended Data Fig. 6b,f), supporting the inhibition of hTRPV3-G573S by the binding of Trpvicin to the VSLD-PD site. Notably, the structures revealed that the dilated SF and activation gate were caused by the mutation G573S. G573 is located at the beginning of the S4–S5 linker helix, which, together with the TRP helix, serves as a gearbox-like unit important for channel gating (Fig. 4d). A closer look at the G573S mutation site reveals that G573S alters the interaction between the hinge of the S4–S5 linker and the TRP helix, causing conformational shifts of the S4–S5 linker and the TRP helix through the conserved W692 (Fig. 4d, right panel). Compared to hTRPV3$_{\text{apo}}$, the shift of the TRP helix expands the activation gate via direct connection to the S6 helix. Moreover, the shift of the S4–S5 linker drags the VSLD moving toward the cytosol side, which, in turn, induces the expansion of the SF through interactions with the adjacent PD at the extracellular side (Fig. 4d). These observations elucidate that the G573S mutation alters the gating property of TRPV3 by expanding both the SF and the activation gate, resulting in the constantly open activity of the mutant, which consequently causes OS.

Symmetry remodeling and inhibition of G573S-C2 by Trpvicin

Our 2.9-Å cryo-EM structure of hTRPV3-G573S-C2$_{\mathrm{Trpvicin}}$ clearly reveals additional pore binding sites for Trpvicin in the central cavity and substantial subunit rearrangements upon Trpvicin binding (Fig. 5). Four Trpvicin molecules bind to the primary VSLD-PD sites of hTRPV3-G573S-C2$_{\mathrm{Trpvicin}}$, which are nearly identical to the hTRPV3$_{\mathrm{Trpvicin}}$ and hTRPV3-G573S-C4$_{\mathrm{Trpvicin}}$ structures (Fig. 5a and Extended Data Fig. 8a–c). Strikingly, six additional pieces of density stacking in three layers were observed in the central cavity of hTRPV3-G573S-C2$_{\mathrm{Trpvicin}}$, which were absent in the hTRPV3$_{\mathrm{apo}}$, hTRPV3$_{\mathrm{Trpvicin}}$ or hTRPV3-G573S-C4$_{\mathrm{Trpvicin}}$ maps (Fig. 5b,d,e and Extended Data Fig. 9c). Six Trpvicin molecules fit well in these densities, manifesting C2 symmetry in each layer (Fig. 5d,e). The two Trpvicins on the top layer directly engage the SF through polar interactions with the main-chain carbonyl oxygens of T636 and I637 (Fig. 5b, right panel). The dimethoxypyrimidine and pyridine groups are parallel to the P-loops from protomers B and D (colored in cyan), comprising the short side of the rectangle SF (Fig. 5b–d). We, therefore, speculate that the top layer Trpvicins are the main driving force for the C4-symmetry to C2-symmetry transition, resulting in the diamond-shaped SF and activation gate with diameters of 8.6 Å × 18.8 Å and 8.8 Å × 13.3 Å, respectively (Fig. 5c,f). Meanwhile, the middle and bottom layer molecules are partially located in the four fenestrations of the pore domains (Extended Data Fig. 8d). Compared to hTRPV3$_{\mathrm{apo}}$, hTRPV3-G573S-C2$_{\mathrm{Trpvicin}}$ showed substantially larger fenestration (Extended Data Fig. 8d), suggesting that the drugs may access the cavity binding sites through the enlarged fenestrations. Once bound, the six Trpvicin molecules physically block the ion path (Fig. 5a,d,e). In addition, antagonist binding in the cavity further alters the channel gating by stabilizing the S6 helices in the α-helical configuration through direct interaction with F666 (Fig. 5d,e and Extended Data Fig. 9a). In the hTRPV3-G573S-C2$_{\mathrm{Trpvicin}}$ structure, the F666 residues from protomers B and D are sandwiched by the top and middle layers of Trpvicin, and the F666 residues from protomers A and C (colored in pink) interact with the bottom layer Trpvicin via π–π stacking (Fig. 5b,d,e). To validate the importance of F666 and T665 for the pore binding sites of Trpvicin, we examined the inhibitory efficacy of Trpvicin on the hTRPV3-G573S-F666A, hTRPV3-G573S-F666Y and hTRPV3-G573S-T665A double mutants. All these double mutants functioned similarly to hTRPV3-G573S but showed a decrease in the potency of Trpvicin by 17-fold, 12-fold and 16-fold, respectively (Extended Data Fig. 6b,f). Interestingly, the single mutations hTRPV3-F666A, hTRPV3-F666Y and hTRPV3-T665A also reduced the potency of Trpvicin by 10-fold, 14-fold and 9-fold (Extended Data Fig. 6c,e), which suggests that the pore binding pocket is important for hTRPV3-WT as well. Collectively, our results not only present a TRPV3 antagonist as a tool compound but also identify drug-binding pockets in TRPV3, providing a template for further rational drug design. Our structures demonstrate that Trpvicin manipulates TRPV3 channel gating through VSLD-PD-binding inhibition, symmetry remodeling and pore blocking.

Discussion

In this study, we identified Trpvicin as a potent and subtype-selective inhibitor of TRPV3. The high-resolution cryo-EM structure of hTRPV3$_{\mathrm{Trpvicin}}$ showed that Trpvicin stabilizes the channel in the closed conformation, elucidating the molecular mechanism of TRPV3 inhibition by Trpvicin (Extended Data Fig. 10a,b). Many TRP channel structures complexed with ligands have provided mechanistic insights into their binding and modulation[4]. Among the TRPV subfamily members, the vanilloid-binding pocket is a conserved ligand-binding pocket[44,45] (Fig. 3c–e). Small molecules, such as cannabidiol, capsazepine, and econazole, displace endogenous lipids from the S4–S5 pocket to alter the channel gating[40]. For other TRPV3 antagonist-binding sites, Liu et al. reported that the clinical medication dyclonine exerts inhibitory effect on TRPV3 to decrease skin inflammation. Their studies suggested that the key residues for dyclonine binding are probably located in the TRPV3 pore region[46]. Neuberger et al. recently reported the cryo-EM structure of TRPV3 in complex with dyclonine and found that dyclonine binds inside the portals of the pore domain that connect the membrane environment to the central cavity of the ion channel pore[47]. However, because of the relatively low affinity of dyclonine to TRPV3 and lack of clear density to accurately assign the orientation of dyclonine, this structure provides limited information for structure-based drug optimization. The structure of mTRPV3$_{\mathrm{Y564A}}$ in complex with plant-derived coumarin osthole revealed two types of osthole-binding sites in TRPV3, which are thought to coincide with 2-APB. To date, osthole and its derivatives have limitations for disease treatment due to the high concentration needed and their action on numerous targets[31]. Here, we showed that the TRPV3 antagonist Trpvicin binds in the vanilloid extended pocket (Fig. 3e). In addition, we also showed the effectiveness of Trpvicin in relieving OS-like symptoms in mouse models. Nevertheless, especially in the chronic itch and hair loss mouse models, a PK study of mouse skin would be needed for the further detection of drug exposure to ensure that the observed efficacy is due to the blocking of TRPV3 by Trpvicin.

The S4–S5 linker and TRP helix have been proposed to play important roles in gating transitions[48,49]. A gearbox-like model has been proposed for TRP channel gating controlled by the coupling of the TRP helix and the S4–S5 linker[50]. However, how the conformational changes of the TRP helix couple to the channel gating remained elusive before this work. The hTRPV3-G573S structures revealed that conformational changes at the TRP helix caused by the G573S mutation are propagated to the activation gate through the pore-lining S6 helices. Meanwhile, the G573S-induced conformational changes also propagate indirectly to the SF through the VSLD, which expands both the activation gate and the SF (Extended Data Fig. 10c,d). The S6 helix has been shown to adopt different conformations in TRPV3 state transitions—for example, a π-helical conformation in the closed and open states and an α-helical configuration in the inactivated state[30]. Such α-helical and π-helical conformations of S6 helices were also observed in our structures.

The binding poses of Trpvicin in the VSLD-PD site of the G573S mutant appear nearly identical to that in the closed-state hTRPV3-WT, which suggests that Trpvicin binding at this VSLD-PD site is probably state-independent. Even though the ion path of hTRPV3-G573S-C4$_{\mathrm{Trpvicin}}$ is larger than that of hTRPV3$_{\mathrm{apo}}$, it is not fully open. This finding supports the observation that Trpvicin binding at the VSLD-PD site prevents channel opening. We identified additional sites inside the central cavity of hTRPV3-G573S-C2$_{\mathrm{Trpvicin}}$. The antagonist likely accesses the cavity through the fenestration or the open activation gate. Mutations of the pore binding site residues on hTRPV3-WT showed a similar decrease in the potency of Trpvicin for hTRPV3-G573S, which suggests that Trpvicin can also bind to the pore binding sites of hTRPV3-WT once access is available. Because the binding of Trpvicin to the VSLD-PD site of hTRPV3-WT already trapped the channel in the closed state, no Trpvicin was observed in the central cavity of the TRPV3-WT structure. For G568V, we observed a decrease in the IC$_{50}$ of Trpvicin. G568 is located at the end of S4, with only two helical turns below A560, the critical residue for Trpvicin binding. Mutation of G568 to Val might cause a conformational change in the VSLD-PD pocket, thus influencing Trpvicin binding to this site. Taken together, our results elucidate the inhibition of TRPV3 by Trpvicin and provide important mechanistic insights into the pathogenic mutation, S4–S5 linker, TRP helix-mediated gating, VSLD-PD-binding site and pore blocking of TRPV3 by the same antagonist. The mode of action of Trpvicin and molecular mechanisms of the human-disease-related TRPV3 mutant channel that we show here will set the stage for drug development.

Online content

Any methods, additional references, Nature Research reporting summaries, source data, extended data, supplementary information, acknowledgements, peer review information; details of author contributions and competing interests; and statements of data and code availability are available at https://doi.org/10.1038/s41589-022-01166-5.

References

1. Bautista, D. M., Wilson, S. R. & Hoon, M. A. Why we scratch an itch: the molecules, cells and circuits of itch. *Nat. Neurosci.* **17**, 175–182 (2014).
2. Xie, Z. & Hu, H. TRP channels as drug targets to relieve itch. *Pharmaceuticals (Basel)* **11**, 100 (2018).
3. Huang, C. C. et al. A histamine-independent itch pathway is required for allergic ocular itch. *J. Allergy Clin. Immunol.* **137**, 1267–1270 (2016).
4. Koivisto, A.P., Belvisi, M.G., Gaudet, R. & Szallasi, A. Advances in TRP channel drug discovery: from target validation to clinical studies. *Nat. Rev. Drug Discov.* **21**, 41–59 (2021).
5. Moore, C., Gupta, R., Jordt, S. E., Chen, Y. & Liedtke, W. B. Regulation of pain and itch by TRP channels. *Neurosci. Bull.* **34**, 120–142 (2018).
6. Kittaka, H. & Tominaga, M. The molecular and cellular mechanisms of itch and the involvement of TRP channels in the peripheral sensory nervous system and skin. *Allergol. Int.* **66**, 22–30 (2017).
7. Clapham, D. E. TRP channels as cellular sensors. *Nature* **426**, 517–524 (2003).
8. Ramsey, I. S., Delling, M. & Clapham, D. E. An introduction to TRP channels. *Annu. Rev. Physiol.* **68**, 619–647 (2006).
9. van Goor, M. K., de Jager, L., Cheng, Y. & van der Wijst, J. High-resolution structures of transient receptor potential vanilloid channels: unveiling a functionally diverse group of ion channels. *Protein Sci.* **29**, 1569–1580 (2020).
10. Smith, G. D. et al. TRPV3 is a temperature-sensitive vanilloid receptor-like protein. *Nature* **418**, 186–190 (2002).
11. Vay, L., Gu, C. & McNaughton, P. A. The thermo-TRP ion channel family: properties and therapeutic implications. *Br. J. Pharmacol.* **165**, 787–801 (2012).
12. Xu, H. et al. TRPV3 is a calcium-permeable temperature-sensitive cation channel. *Nature* **418**, 181–186 (2002).
13. Sherkheli, M. A., Vogt-Eisele, A. K., Weber, K. & Hatt, H. Camphor modulates TRPV3 cation channels activity by interacting with critical pore-region cysteine residues. *Pak. J. Pharm. Sci.* **26**, 431–438 (2013).
14. Chung, M. K., Lee, H., Mizuno, A., Suzuki, M. & Caterina, M. J. 2-aminoethoxydiphenyl borate activates and sensitizes the heat-gated ion channel TRPV3. *J. Neurosci.* **24**, 5177–5182 (2004).
15. Peier, A. M. et al. A heat-sensitive TRP channel expressed in keratinocytes. *Science* **296**, 2046–2049 (2002).
16. Cheng, X. et al. TRP channel regulates EGFR signaling in hair morphogenesis and skin barrier formation. *Cell* **141**, 331–343 (2010).
17. Aijima, R. et al. The thermosensitive TRPV3 channel contributes to rapid wound healing in oral epithelia. *FASEB J.* **29**, 182–192 (2015).
18. Asakawa, M. et al. Association of a mutation in TRPV3 with defective hair growth in rodents. *J. Invest. Dermatol.* **126**, 2664–2672 (2006).
19. Yamamoto-Kasai, E. et al. TRPV3 as a therapeutic target for itch. *J. Invest. Dermatol.* **132**, 2109–2112 (2012).
20. Xiao, R., Tian, J., Tang, J. & Zhu, M. X. The TRPV3 mutation associated with the hairless phenotype in rodents is constitutively active. *Cell Calcium* **43**, 334–343 (2008).
21. Lin, Z. et al. Exome sequencing reveals mutations in TRPV3 as a cause of Olmsted syndrome. *Am. J. Hum. Genet.* **90**, 558–564 (2012).
22. Zhao, J. et al. PAR2 mediates itch via TRPV3 signaling in keratinocytes. *J. Invest. Dermatol.* **140**, 1524–1532 (2020).
23. Phelps, C. B., Wang, R. R., Choo, S. S. & Gaudet, R. Differential regulation of TRPV1, TRPV3, and TRPV4 sensitivity through a conserved binding site on the ankyrin repeat domain. *J. Biol. Chem.* **285**, 731–740 (2010).
24. Nadezhdin, K. D. et al. Structural mechanism of heat-induced opening of a temperature-sensitive TRP channel. *Nat. Struct. Mol. Biol.* **28**, 564–572 (2021).
25. Singh, A. K., McGoldrick, L. L. & Sobolevsky, A. I. Structure and gating mechanism of the transient receptor potential channel TRPV3. *Nat. Struct. Mol. Biol.* **25**, 805–813 (2018).
26. Singh, A. K. et al. Structural basis of temperature sensation by the TRP channel TRPV3. *Nat. Struct. Mol. Biol.* **26**, 994–998 (2019).
27. Zubcevic, L. et al. Conformational ensemble of the human TRPV3 ion channel. *Nat. Commun.* **9**, 4773 (2018).
28. Zubcevic, L., Borschel, W. F., Hsu, A. L., Borgnia, M. J. & Lee, S. Y. Regulatory switch at the cytoplasmic interface controls TRPV channel gating. *eLife* **8**, e47746 (2019).
29. Shimada, H. et al. The structure of lipid nanodisc-reconstituted TRPV3 reveals the gating mechanism. *Nat. Struct. Mol. Biol.* **27**, 645–652 (2020).
30. Deng, Z. et al. Gating of human TRPV3 in a lipid bilayer. *Nat. Struct. Mol. Biol.* **27**, 635–644 (2020).
31. Neuberger, A., Nadezhdin, K. D., Zakharian, E. & Sobolevsky, A. I. Structural mechanism of TRPV3 channel inhibition by the plant-derived coumarin osthole. *EMBO Rep.* **22**, e53233 (2021).
32. Gomtsyan, A. et al. Synthesis and pharmacology of (pyridin-2-yl) methanol derivatives as novel and selective transient receptor potential vanilloid 3 antagonists. *J. Med. Chem.* **59**, 4926–4947 (2016).
33. Sun, X. Y. et al. Antipruritic effect of natural coumarin osthole through selective inhibition of thermosensitive TRPV3 channel in the skin. *Mol. Pharmacol.* **94**, 1164–1173 (2018).
34. Black, L. B. et al. N-(1,3-Thiazol-2-yl) pyrimidine-5-carboxamides as TRPV3 modulators and their preparation. https://patents.google.com/patent/WO2016160938A1/un (2016).
35. Cahusac, P. M. Effects of transient receptor potential (TRP) channel agonists and antagonists on slowly adapting type II mechanoreceptors in the rat sinus hair follicle. *J. Peripher. Nerv. Syst.* **14**, 300–309 (2009).
36. Oetjen, L. K. et al. Sensory neurons co-opt classical immune signaling pathways to mediate chronic itch. *Cell* **171**, 217–228 (2017).
37. Song, Z. et al. Hair loss caused by gain-of-function mutant TRPV3 is associated with premature differentiation of follicular keratinocytes. *J. Invest. Dermatol.* **141**, 1964–1974 (2021).
38. Goehring, A. et al. Screening and large-scale expression of membrane proteins in mammalian cells for structural studies. *Nat. Protoc.* **9**, 2574–2585 (2014).
39. Ding, K. et al. Observing noncovalent interactions in experimental electron density for macromolecular systems: a novel perspective for protein–ligand interaction research. *J. Chem. Inf. Model.* **62**, 1734–1743 (2022).
40. Zhao, Y., McVeigh, B. M. & Moiseenkova-Bell, V. Y. Structural pharmacology of TRP channels. *J. Mol. Biol.* **433**, 166914 (2021).
41. Zubcevic, L., Hsu, A. L., Borgnia, M. J. & Lee, S. Y. Symmetry transitions during gating of the TRPV2 ion channel in lipid membranes. *eLife* **8**, e45779 (2019).
42. Hughes, T. E. T. et al. Structural insights on TRPV5 gating by endogenous modulators. *Nat. Commun.* **9**, 4198 (2018).

43. Dang, S. et al. Structural insight into TRPV5 channel function and modulation. *Proc. Natl Acad. Sci. USA* **116**, 8869–8878 (2019).
44. Gao, Y., Cao, E., Julius, D. & Cheng, Y. TRPV1 structures in nanodiscs reveal mechanisms of ligand and lipid action. *Nature* **534**, 347–351 (2016).
45. Cao, E., Liao, M., Cheng, Y. & Julius, D. TRPV1 structures in distinct conformations reveal activation mechanisms. *Nature* **504**, 113–118 (2013).
46. Liu, Q. et al. Therapeutic inhibition of keratinocyte TRPV3 sensory channel by local anesthetic dyclonine. *eLife* **10**, e68128 (2021).
47. Neuberger, A., Nadezhdin, K. D. & Sobolevsky, A. I. Structural mechanism of TRPV3 channel inhibition by the anesthetic dyclonine. *Nat. Commun.* **13**, 2795 (2022).
48. Pumroy, R. A., Fluck, E. C. 3rd, Ahmed, T. & Moiseenkova-Bell, V. Y. Structural insights into the gating mechanisms of TRPV channels. *Cell Calcium* **87**, 102168 (2020).
49. Zhang, K., Julius, D. & Cheng, Y. Structural snapshots of TRPV1 reveal mechanism of polymodal functionality. *Cell* **184**, 5138–5150 (2021).
50. Hofmann, L. et al. The S4–S5 linker—gearbox of TRP channel gating. *Cell Calcium* **67**, 156–165 (2017).

Methods

Plasmid constructs

The full-length cDNA of hTRPV3 (791 amino acids (aa)) (NM_001258205.2), hTRPV1 (NM_018727.5), hTRPV4 (NM_001177431.1), hTRPV5 (NM_019841.7) and hTRPV6 (NM_018646.6) were amplified from HEK293 cDNA library, whereas cDNA of mTRPV3 (NM_145099.2), mTRPV2 (NM_011706.2), hTRPA1 (NM_007332.2) and hTRPM8 (NM_024080.4) were purchased from MiaoLing Plasmid Sharing Platform. Then, most of these genes were cloned into a pEG BacMam vector fused with a GFP-twin-Strep tag at the C-terminus, except for hTRPA1 and hTRPM8, which were cloned into a pIRES2-EGFP vector with an EGFP tag translated separately. All hTRPV3 and mTRPV3 mutants were generated by site-directed mutagenesis. The primer information is included in Supplementary Table 3. All constructs used in this study were confirmed by DNA sequencing.

Cell culture, high-throughput screening with cell viability assay and safety screen

HEK293T cells were cultured in DMEM containing 10% FBS (Thermo Fisher Scientific) and 1% penicillin–streptomycin (Thermo Fisher Scientific) at 37 °C with 5% CO_2. The transfection of corresponding plasmids was conducted using Lipofectamine 3000 following the manufacturer's instructions (Invitrogen).

The ~110,000-compound library used for the screening was with >95% purity, and the stock was solubilized in 100% dimethyl sulfoxide (DMSO) with an average concentration of 10 mmol L^{-1} for each compound in 384-well plates. The high-throughput screen of TRPV3 antagonists was conducted as follows: 10 mM stock solutions of the library were transferred into 384-well plates with an Echo 520 Liquid Handler (Labcyte) for a volume of 25 nl for each molecule. This was followed by seeding ~1,000 HEK293T cells per well into the 384-well plates in the form of 25-µl suspension containing hTRPV3-G573S plasmid and Lipofectamine 3000 reagents with a MultiDrop Combi Reagent Dispenser (Thermo Fisher Scientific). After being cultured for 24 hours at 37 °C, 5% CO_2 and 95% humidity, the cell viability was tested with CellTiter-Glo Luminescent Cell Viability Assay following the standard protocol suggested by the manufacturer (Promega) (Supplementary Table 4).

For evaluation of off-target effects, Trpvicin at 10 µM in duplicate was screened for the 47 safety panel following the manufacturer's instructions with a commercial screen (SafetyScreen 47, ICE Bioscience). The binding was calculated as a percent activation or inhibition of the positive control ligands specific for each target. The compound enzyme inhibition effect was calculated as a percent inhibition of control enzyme activity (Supplementary Table 1 and Supplementary Fig. 3).

Electrophysiology

Electrophysiological experiments were performed 12–24 hours after transfection. Whole-cell patch-clamp recordings were carried out using an EPC10 amplifier with PatchMaster software (HEKA). Electrodes were pulled from borosilicate glass with a P-97 micropipette puller (Sutter Instrument), and those with resistances of 3–5 MΩ were used for experiments. An Ag-AgCl wire was used as a reference electrode, and signals were filtered using a 2.9-kHz low-pass Bessel filter. Cell membrane capacitances were monitored and used to calculate current densities. Membrane potential was held at 0 mV. For recording of agonist-induced activation and inhibition by Trpvicin or RR, currents were elicited by a protocol consisting of a 400-ms step to +80 mV, followed by a 400-ms step to −80 mV at 2-second intervals. Only for the recording of hTRPM8, pipette solutions contained 50 mM CsCl, 10 mM NaCl, 10 mM HEPES, 60 mM CsF and 20 mM EGTA (buffered to pH 7.2 with CsOH), and bath solutions contained 140 mM NaCl, 3.5 mM KCl, 1 mM $MgCl_2 \cdot 6H_2O$, 10 mM D-glucose, 10 mM HEPES and 1.25 mM $NaH_2PO_4 \cdot 2H_2O$ (buffered to pH 7.4 with NaOH). For the recording of other channels, including hTRPV3, mTRPV3 as well as variants of TRPV3, hTRPV1, mTRPV2, hTRPV4, hTRPV5, hTRPV6 and hTRPA1, both pipette and bath solutions contained 130 mM NaCl, 0.3 mM EDTA and 3 mM HEPES (buffered to pH 7.4 with NaOH). To circumvent the cell toxicity of TRPV3 gain-of-function mutations, their recordings were carried out usually 12 hours after transfection. Chemicals, including all agonists and RR, were purchased from Sigma-Aldrich. All recordings were made at room temperature.

Animal experiments

All mouse experiments were approved by the Institutional Animal Care and Use Committees of Peking University First Hospital in Beijing, China. Adult wild-type male C57BL/6J mice at age of 8–12 weeks were purchased from SiPeiFu Biotechnology. Trpv3 knock-in mice (*Trpv3*$^{+/G568V}$) were generated through embryonic stem cell targeting by Cyagen Biosciences. Mice were all housed in a controlled environment at 24 ± 2 °C, with a 12-hour light/dark cycle and 50 ± 10% humidity. Food and water were available ad libitum.

The pharmacokinetics of Trpvicin was tested by a single intravenous (i.v.) injection or oral administration (p.o.) in 8-week-old male CD-1 mice ($n = 3$) at a dose of 2.5 mg kg^{-1} and 10 mg kg^{-1}, respectively. Blood samples were collected at 0.083, 0.25, 1, 2, 4, 6, 8, 24 and 48 hours after administration through orbital venous plexus by capillary, EDTA-K2 anticoagulant. The blood samples were quantified by liquid chromatography with tandem mass spectrometry (LC–MS/MS), and data analysis was conducted using PKsolver2.0.

To assess itch scratching behavior, wild-type male C57BL/6J mice at 8–12 weeks of age were put in an observation box (15 × 10 × 15 cm^3), and their scratching behavior was video-recorded. The number of scratching bouts was counted afterwards through video playback analysis. One scratching bout was defined as one instance of raising a hindlimb and continuously scratching for any time length before returning the limb to the floor or animal's mouth. For the acute itch test, the hair of the rostral part of the mouse neck was shaved at least 2 days before behavioral testing. Then, 50 µg of SLIGRL (GenScript) was dissolved in 50 µl of 0.9% saline and injected intradermally at the left or right side of the nape to elicit acute itch. Trpvicin was first dissolved in DMSO and then diluted with saline to a final DMSO concentration of no more than 0.1% for intradermal injections. On testing days, mice were pre-injected with vehicle (0.1% DMSO) or different concentrations of Trpvicin 30 minutes before intradermal injection of SLIGRL. Scratching behavior was quantified by recording the number of scratching bouts in 30 minutes. In the chronic itch model of AD, mice were topically treated once a day with 20 µl of 100 µM MC903 (calcipotriol, Tocris Bioscience) dissolved in ethanol for 7 days on both ears. Trpvicin dissolved in DMSO was diluted with PEG400 to a final DMSO concentration of no more than 7%. Mice were gavaged with vehicle (7% DMSO) or different concentrations of Trpvicin once daily starting from 5 days before topical treatment of MC903. Scratching behavior was quantified by recording 1 hour before the daily MC903 treatment on the 1st, 4th and 8th day of AD modeling. Ear thickness was measured with dial calipers.

To assess the effect of Trpvicin on knock-in mice with the gain-of-function mutant TRPV3, *Trpv3*$^{+/G568V}$ littermate mice were topically treated once a day with the homemade cream containing 1 wt% Trpvicin or vehicle alone (12 wt% glycerol, 3 wt% peregal, 10 wt% stearyl alcohol, 12 wt% monoglyceride, 5 wt% isooctyl palmitate, 8 wt% liquid paraffin and water added up to 100%) on the back starting from P50. Mice were anesthetized with 2.5 wt% tribromoethanol (Sigma-Aldrich) and photographed every 4 days. To compare the coverage of black fur between groups quantitatively, all photographs were first converted to the 8-bit type and then analyzed by ImageJ to calculate the inverted mean gray value of the back area of every mouse.

Protein expression and purification

The recombinant baculovirus was generated in insect Sf9 cells following the manufacturer's protocol. P2 viruses were used to infect HEK293F GnTI$^-$ cells at 2 × 10^6 cells ml^{-1}. To minimize the cytotoxicity caused by the constitutive activity of the hTRPV3-G573S, 10 µM

Trpvicin was added into the medium during the expression of the hTRPV3-G573S protein. After 8–10 hours of culture at 37 °C, 10 mM sodium butyrate was added to boost protein expression. Cells were harvested 48 hours later by centrifugation at 1,800*g* and were frozen until further purification.

The whole purification process was carried out either on ice or at 4 °C. Cells were resuspended in lysis buffer A (20 mM Tris, 150 mM NaCl, pH 8.0) supplemented with protease inhibitors, including 250 µM phenylmethylsulfonyl fluoride (PMSF), 0.8 µM aprotinin, 4.7 µM leupeptin, 2 µM pepstatin A and 2 mM β-mercaptoethanol (β-ME). Cells were disrupted by the Dounce homogenizer, and then membrane debris was collected by ultracentrifugation for 1.5 hours (Beckman, Ti32 rotor, 100,000 *g*). The membrane fraction was homogenized and resuspended in buffer A supplemented with 1% (w/v) dodecyl-β-d-maltopyranoside (DDM) (Jiejing Tech) plus 0.2% CHS (Anatrace) and was slowly stirred for 2 hours. The supernatant was collected by another 40-minute ultra-centrifugation and passed through a 0.22-µm filter before loading onto the gravitate column packed with Streptactin Beads (Smart-Lifesciences). The resin was then washed with 10 column volumes of buffer A supplemented with 0.06% (w/v) GDN (Anatrace). Protein was eluted with buffer A containing 0.06% (w/v) GDN and 5 mM desthiobiotin (Sigma-Aldrich). The eluted sample was concentrated and loaded onto a Superose 6 column (GE Healthcare) equilibrated with buffer A plus 0.007% (w/v) GDN. Peak fractions corresponding to the tetrameric TRPV3 were pooled and concentrated to ~10 mg ml^{-1} for cryo-EM sample preparation.

Except for the TRPV3$_{apo}$, the expression and purification processes were supplemented with 10 µM Trpvicin, and an additional 100 µM Trpvicin was added to the final concentrated protein sample.

Cryo-EM grid preparation and data collection

A droplet of 3 µl of hTRPV3-WT or hTRPV3-G573S was applied onto a glow-discharged gold grid (Quantifoil R1.2/1.3). The grid was then blotted for 2.0–4.0 seconds at 4 °C and 100% humidity using Vitrobot Mark IV (Thermo Fisher Scientific) and flash-frozen in liquid ethane cooled by liquid nitrogen. Cryo-EM data were collected on a FEI Titan Krios (Thermo Fisher Scientific) electron microscope operating at an acceleration voltage of 300 kV using a K2 Summit or K3 direct electron detector positioned after a GIF quantum energy filter (Gatan). Raw movies were automatically acquired in super-resolution mode with a physical pixel size of 1.04 Å for the K2 detector and 1.09 Å for the K3 detector using SerialEM. Each movie stack was recorded for 6.4-second fractionated into 32 frames with a total accumulated dose of ~60 e/Å^2. A total of 2,199, 3,203 and 2,594 movie stacks were collected for hTRPV3$_{apo}$, hTRPV3$_{Trpvicin}$ and hTRPV3-G573S, respectively.

Image processing

All the movie stacks were motion-corrected, binned by two-fold and dose-weighted using MotionCorr2 (ref. [51]). Defocus values of the resulting summed micrographs were estimated with Gctf[52]. Template particle picking, 2D and 3D classification, particle polishing and CTF refinement were carried out in Relion3 (ref. [53]). The final best class contained 347,665, 503,757, 48,492 and 152,978 for hTRPV3$_{apo}$, hTRPV3$_{Trpvicin}$, hTRPV3-G573S-C4$_{Trpvicin}$ and hTRPV3-G573S-C2$_{Trpvicin}$, were imported in cryoSPARC[54] and were refined to 3.54 Å, 2.53 Å, 3.64 Å and 2.93 Å, respectively. Detailed data processing diagrams are presented in Extended Data Figs. 3 and 7.

Model building

The structure of human TRPV3 (Protein Data Bank (PDB) code: 6MHO) was fitted in the cryo-EM density map of hTRPV3$_{apo}$ using Chimera[55]. The fitted model was manually inspected and corrected in COOT[56] and subsequently refined in real space using Phenix[57]. The refined hTRPV3$_{apo}$ model was further used as a template for generating and refining models for the other three structures in this study. Statistics for cryo-EM data collection and model refinement are summarized in Supplementary Table 5.

All figures were prepared with PyMOL (Schrödinger)[58] and ChimeraX[59].

Statistical analyses

All patch-clamp recordings were analyzed using the Igor Pro software. Cure fitting analyses and statistical analyses of itch behavior experiments were performed using GraphPad Prism 8.4.0 software. All values are expressed as mean ± s.e.m. Two-tailed paired Student's *t*-tests and one-way or two-way ANOVA followed by Bonferroni post tests were used to examine statistical significance: $^*P < 0.05$; $^{**}P < 0.01$; $^{***}P < 0.001$.

MM/GBSA calculation

We used the ff14SB force field parameter set for the protein and the gaff force field parameter set for the ligand, using the Leap module of AmberTools21 (ref. [60]). Implicit solvents in the system are simulated by Generalized Born model. MD simulations were performed according to the following steps. (1) Minimization was performed with a maximum cycle of 10,000 and with the steepest descent algorithm for the first 5,000 cycles. (2) The system was heated up to 298 K, and, in this process, all protein backbone atoms are restrained to their original position with a 2.5 kcal/Å restraint force. (3) A 10-ns equilibrium process was performed with a constant temperature of 298 K, and, in this process, all protein backbone atoms are restrained to their original position with a 2.5 kcal/Å restraint force to maintain the binding environment of protein and ligand. Then, the trajectory was used for MM/GBSA binding affinity calculations and decompositions in the Amber 20 program. Entropic contributions were not calculated.

Reporting summary

Further information on research design is available in the Nature Research Reporting Summary linked to this article.

Data availability

The cryo-EM maps for hTRPV3$_{apo}$, hTRPV3$_{Trpvicin}$, hTRPV3-G573S-C4$_{Trpvicin}$ and hTRPV3-G573S-C2$_{Trpvicin}$ have been deposited in the Electron Microscopy Data Bank with accession codes EMD-33218, EMD-33214, EMD-33217 and EMD-33216. Atomic coordinates for hTRPV3$_{apo}$, hTRPV3$_{Trpvicin}$, hTRPV3-G573S-C4$_{Trpvicin}$ and hTRPV3-G573S-C2$_{Trpvicin}$ have been deposited in the Protein Data Bank under accession codes 7XJ3, 7XJ0, 7XJ2 and 7XJ1. Source data are provided with this paper.

References

51. Zheng, S. Q. et al. MotionCor2: anisotropic correction of beam-induced motion for improved cryo-electron microscopy. *Nat. Methods* **14**, 331–332 (2017).
52. Zhang, K. Gctf: real-time CTF determination and correction. *J. Struct. Biol.* **193**, 1–12 (2016).
53. Zivanov, J. et al. New tools for automated high-resolution cryo-EM structure determination in RELION-3. *eLife* **7**, e42166 (2018).
54. Punjani, A., Rubinstein, J. L., Fleet, D. J. & Brubaker, M. A. cryoSPARC: algorithms for rapid unsupervised cryo-EM structure determination. *Nat. Methods* **14**, 290–296 (2017).
55. Pettersen, E. F. et al. UCSF Chimera—a visualization system for exploratory research and analysis. *J. Comput. Chem.* **25**, 1605–1612 (2004).
56. Emsley, P. & Cowtan, K. Coot: model-building tools for molecular graphics. *Acta Crystallogr. D Biol. Crystallogr.* **60**, 2126–2132 (2004).
57. Adams, P. D. et al. PHENIX: a comprehensive Python-based system for macromolecular structure solution. *Acta Crystallogr. D Biol. Crystallogr.* **66**, 213–221 (2010).
58. DeLano, W. L. PyMOL: an open-source molecular graphics tool. CCP4 Newsl. Protein Crystallogr. 40, 82–92. http://legacy.ccp4.ac.uk/newsletters/newsletter40/11_pymol.pdf (2002).

59. Pettersen, E. F. et al. UCSF ChimeraX: structure visualization for researchers, educators, and developers. *Protein Sci.* **30**, 70–82 (2021).
60. Case, D. A. et al. Amber 2022 Reference Manual. https://ambermd.org/doc12/Amber22.pdf (2022).

Acknowledgements

We thank X. Huang, B. Zhu, X. Li and L. Chen at the Center for Biological Imaging, Core Facilities for Protein Science, at the Institute of Biophysics, Chinese Academy of Sciences, for support in cryo-EM data collection. Cryo-EM data collection was also supported by the Cryo-EM platform of Peking University with the assistance of Z. Guo, X. Pei, G. Wang, C. Qin and N. Li. We thank W. Guo, Q. Luo and Y. Huang for helpful discussion as well as N. Zheng, M. Liao, L. Chen and H. Hu for proofreading the manuscript. This work is funded by grants from the National Key Research and Development Program of China (2017YFA0505200 to X.L.), the National Natural Science Foundation of China (21625201, 21961142010, 21661140001, 91853202 and 21521003 to X.L.; 82130091 and 81673044 to Y.Y.; and 22177006 to J.F.), the CAMS Innovation Fund for Medical Sciences (2021-1-I2M-018 to Y.Y.), the Beijing Outstanding Young Scientist Program (BJJWZYJH01201910001001 to X.L.) and the Institute of Physics, Chinese Academy of Sciences (E0VK101 to D.J.).

Author contributions

X.L. and Y.Y. initiated the project. X.L., Y.Y. and D.J. supervised the project. J.F. and Z.Y. prepared the samples for the cryo-EM study and made the mutation constructs. D.J. and J.F. collected the cryo-EM data. D.J. calculated the EM maps. D.J. and J.F. built and refined the atomic model. L.H. performed the electrophysiological assays. L.H. and F.G. conducted the high-throughput chemical screening and animal studies. D.L. synthesized all of the compounds. H.K. did the MM/GBSA calculations. X.L., Y.Y., D.J., J.F. and L.H. analyzed the data. All authors contributed to the manuscript preparation.

Competing interests

X.L. and Y.Y. are co-founders of Iongen Therapeutics Co. Ltd., and D.L. is currently a full-time employee of Iongen. The remaining authors declare no competing interests.

Additional information

Extended data is available for this paper at https://doi.org/10.1038/s41589-022-01166-5.

Supplementary information The online version contains supplementary material available at https://doi.org/10.1038/s41589-022-01166-5.

Correspondence and requests for materials should be addressed to Daohua Jiang, Yong Yang or Xiaoguang Lei.

Peer review information *Nature Chemical Biology* thanks Jun Chen, Zhiguang Yuchi and the other, anonymous, reviewer(s) for their contribution to the peer review of this work.

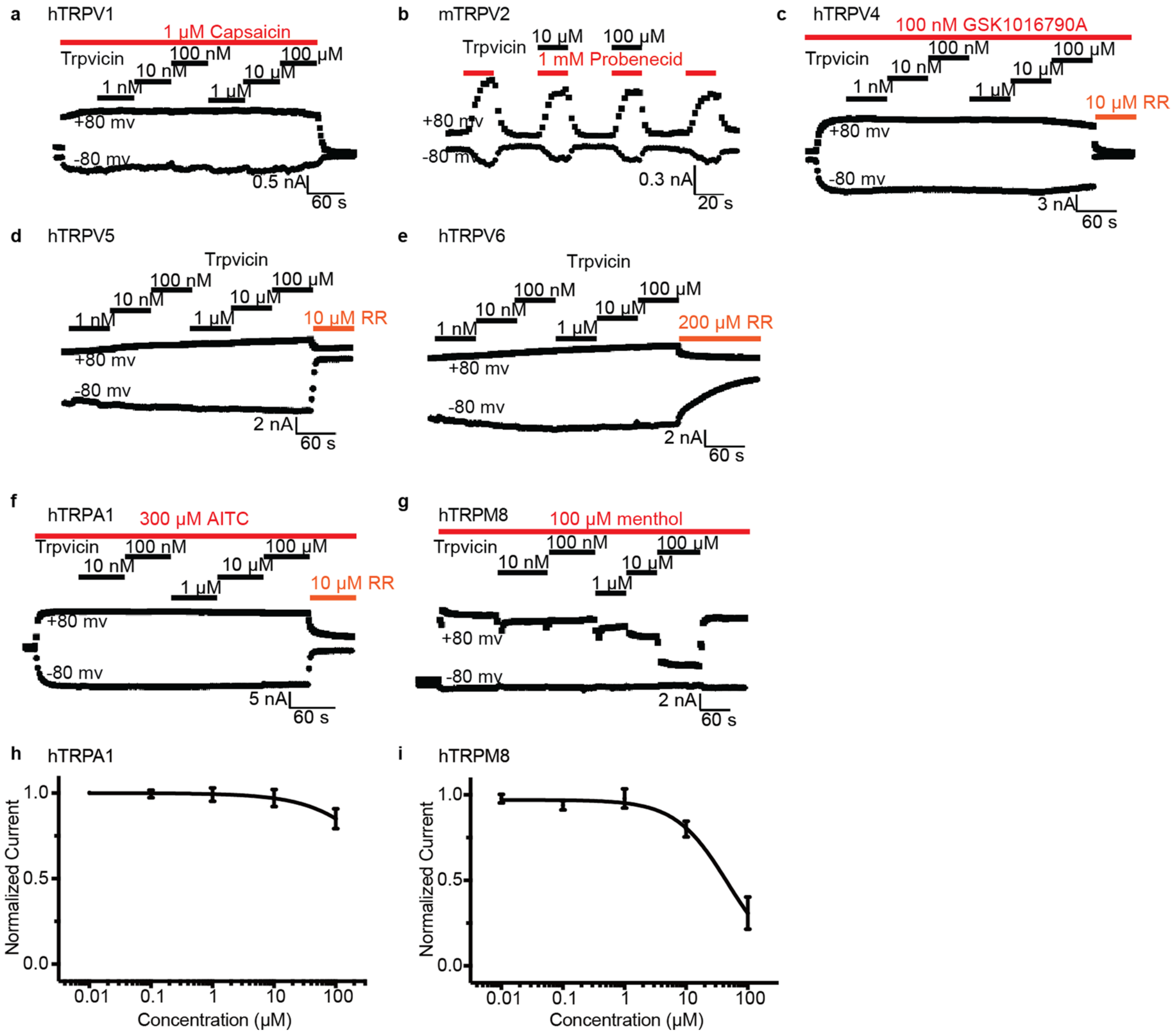

Extended Data Fig. 1 | Trpvicin inhibits TRPV3 in contrast to other representative members of TRP family. a-g, The representative current traces of wild type hTRPV1 (**a**), mTRPV2 (**b**), hTRPV4 (**c**), hTRPV5 (**d**), hTRPV6 (**e**), hTRPA1 (**f**), and hTRPM8 (**g**) inhibited by increasing concentrations of Trpvicin (black bar), at ±80 mV. AITC, allyl-isothiocyanate. **h-i**, Curve fitting of dose-dependent inhibition of agonist-evoked currents by Trpvicin on hTRPA1 (**h**) (300 μM AITC, at −80 mV; logIC$_{50}$ = 3.01 ± 0.75, *n* = 4), and hTRPM8 (**i**) (100 μM menthol, at +80 mV; logIC$_{50}$ = 1.67 ± 0.10, *n* = 3). Data are presented as mean values +/- SEM.

https://doi.org/10.1038/s41589-022-01166-5

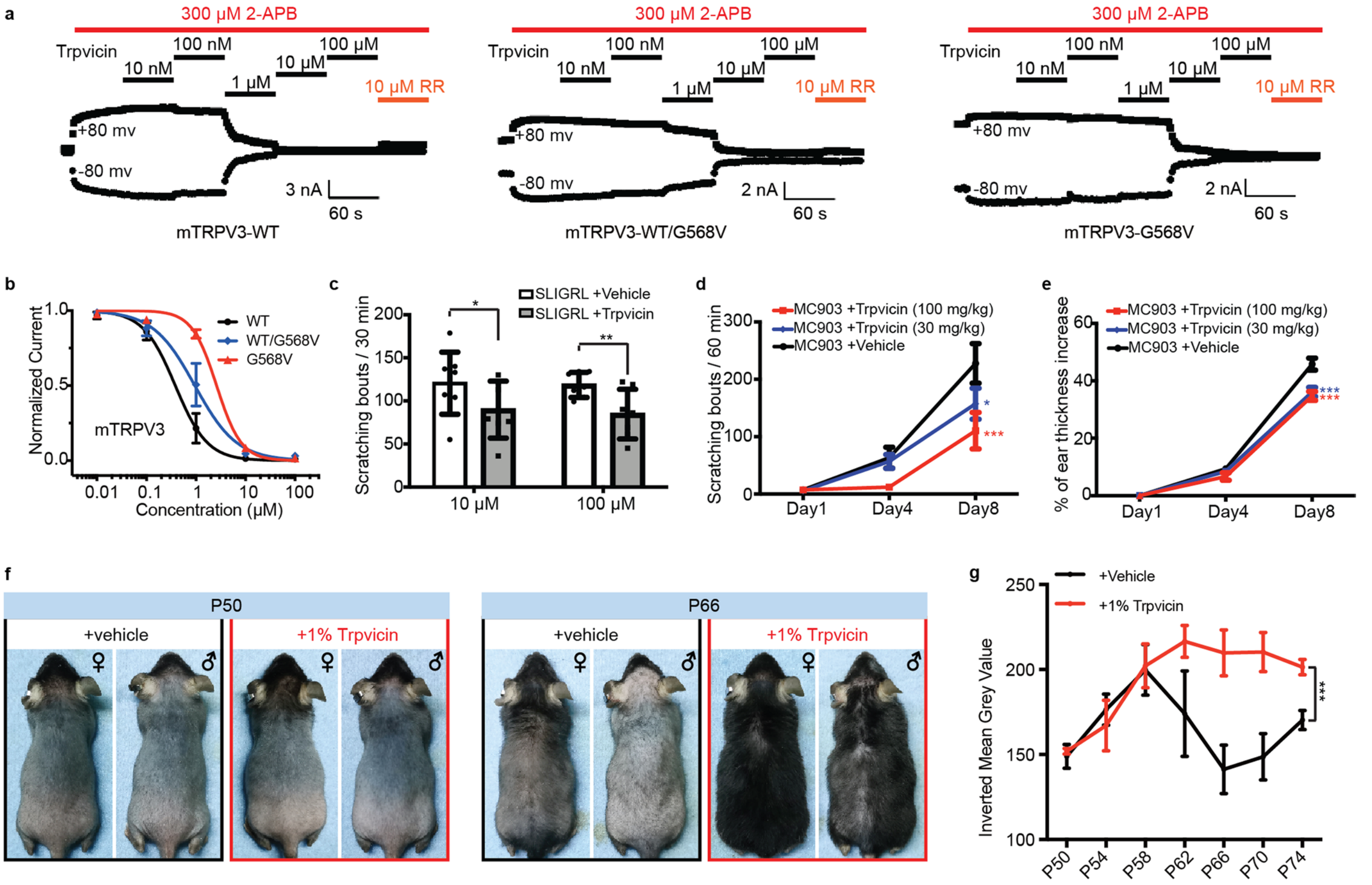

Extended Data Fig. 2 | Trpvicin relieves itch and hair loss in mice. a, The representative current traces of mTRPV3-WT, mTRPV3-WT/G568V, and mTRPV3-G568V in response to 2-APB (300 μM, red bar) and co-application of increasing concentrations of Trpvicin (from 10 nM to 100 μM, black bar), at ±80 mV. 10 μM RR was used to assess the whole amplitudes of leak currents. **b**, Curve fitting of dose-dependent inhibition of 300 μM 2-APB-evoked mTRPV3 WT, WT/G568V, and G568V currents at −80 mV by Trpvicin (mTRPV3-WT, $\log IC_{50} = -0.42 \pm 0.08$, *n* = 5; mTRPV3-WT/G568V, $\log IC_{50} = -0.02 \pm 0.10$, *n* = 5; mTRPV3-G568V, $\log IC_{50} = 0.42 \pm 0.03$, *n* = 7). Data are presented as mean values + /- SEM. **c**, Acute itch behaviors of WT mice induced by intradermal injections of SLIGRL alone or co-application of Trpvicin. Two-sided paired t-tests with the corresponding vehicle-treated groups (10 μM, P = 0.0216; 100 μM, P = 0.0049).*n* = 7. Data are presented as mean values + /- SEM. SLIGRL, peptide SLIGRL-NH_2. **d**,**e**, The scratching bouts (**d**) and percentage of ear thickness increase (**e**) of WT mice treated with MC903 alone or co-application of Trpvicin for 7 days. Two-way ANOVA (**d**, P = 0.0219; **e**, P = 0.0021) followed by Bonferroni post-tests with the vehicle-treated group (+100 mg/kg Trpvicin, *n* = 5; +30 mg/kg Trpvicin, *n* = 8; +Vehicle, *n* = 7). Data are presented as mean values + /- SEM. MC903, calcipotriol. **f**, *Trpv3*$^{+/G568V}$ mice were topically treated with 1 wt% Trpvicin or vehicle once per day starting from P50. After 16 days of treatment, for both genders at P66, the Trpvicin-treated mice showed apparently longer hair shafts in comparison to the vehicle-treated group. **g**, The inverted mean grey values of the back area of *Trpv3*$^{+/G568V}$ mice topically treated with 1 wt% Trpvicin or vehicle starting from P50. Two-way ANOVA compared with the vehicle-treated group, P = 0.0002. *n* = 3. Data are presented as mean values + /- SEM; $^{*}p < 0.05$, $^{**}p < 0.01$, $^{***}p < 0.001$.

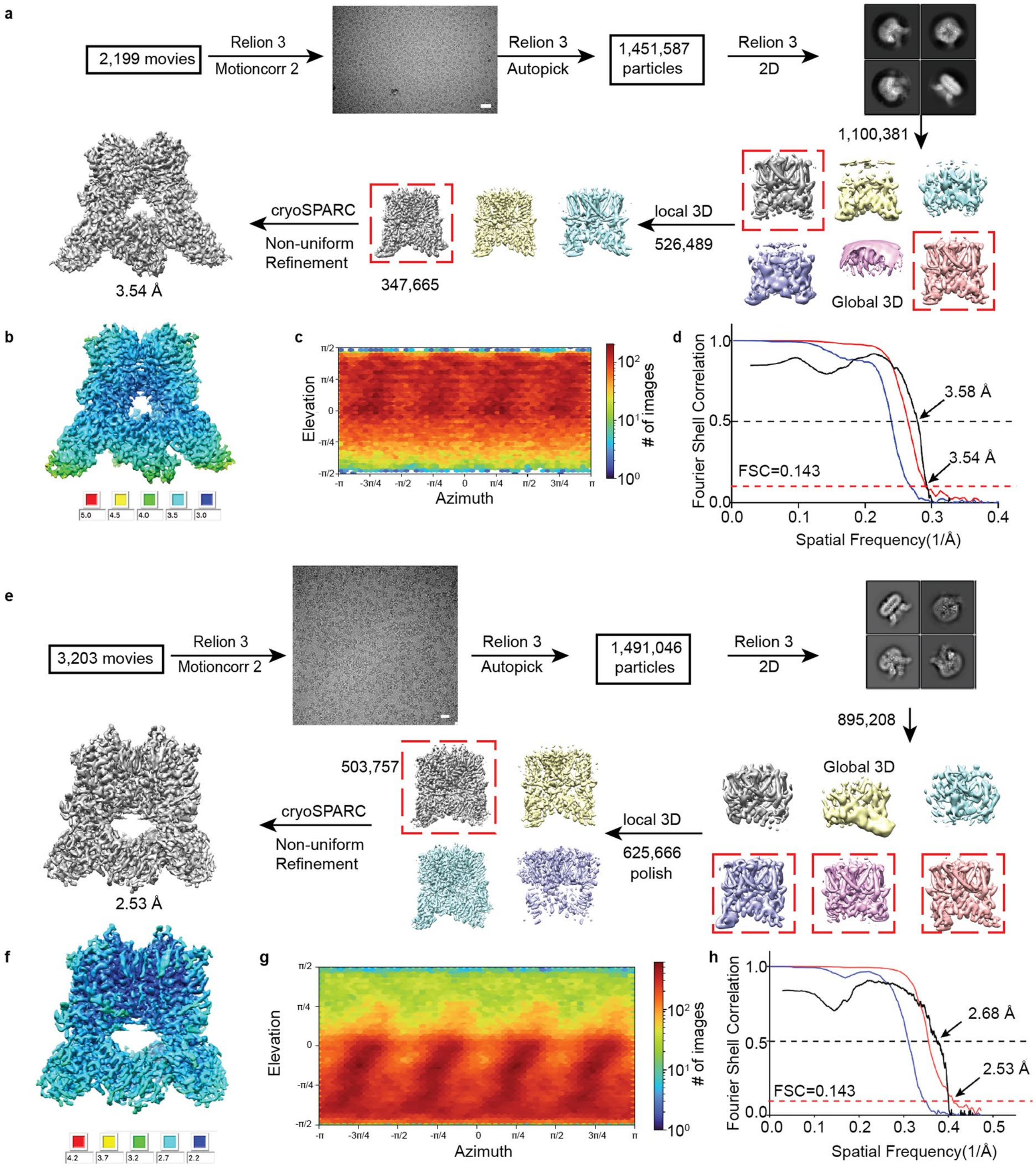

Extended Data Fig. 3 | Cryo-EM data processing of hTRPV3$_{apo}$ and hTRPV3$_{Trpvicin}$. **a**, Flow chart of cryo-EM data processing of hTRPV3$_{apo}$. A total of 1,451,587 particles were picked from 2,199 micrographs. A representative motion-corrected micrograph of the dataset is shown here (Bar = 400 Å). Several rounds of 2D and 3D classifications were conducted to clean particles, followed by Bayesian Polish to improve image quality. The final map was refined at 3.54 Å according to the GSFSC criterion. **b**, Local resolution distribution of the final sharpened map of the hTRPV3$_{apo}$. **c**, Particle angular distribution calculated in cryoSPARC for the final reconstruction. **d**, Fourier Shell Correlations (FSC) of the final map of the hTRPV3$_{apo}$ structure, calculated between two independently refined half-maps before (blue) and after (red) post-processing, overlaid with an FSC curve calculated between the cryo-EM density map and the structural model shown in black. **e**, Flow chart of cryo-EM data processing of hTRPV3$_{Trpvicin}$. A total of 1,491,046 particles were picked from 3,203 micrographs. A representative motion-corrected micrograph is shown here (Bar = 400 Å). Several rounds of 2D and 3D classifications were conducted to clean particles, followed by Bayesian Polish and CTF Refine to improve image quality. The final map was refined at 2.53 Å according to the GSFSC criterion. **f**, Sharpened map of the hTRPV3$_{Trpvicin}$, colored based on the local resolution values. **g**, Particle angular distribution calculated in cryoSPARC for the final reconstruction. **h**, Fourier Shell Correlations (FSC) of the final map of the hTRPV3$_{Trpvicin}$, calculated between two independently refined half-maps before (blue) and after (red) post-processing, overlaid with an FSC curve calculated between the cryo-EM density map and the structural model shown in black.

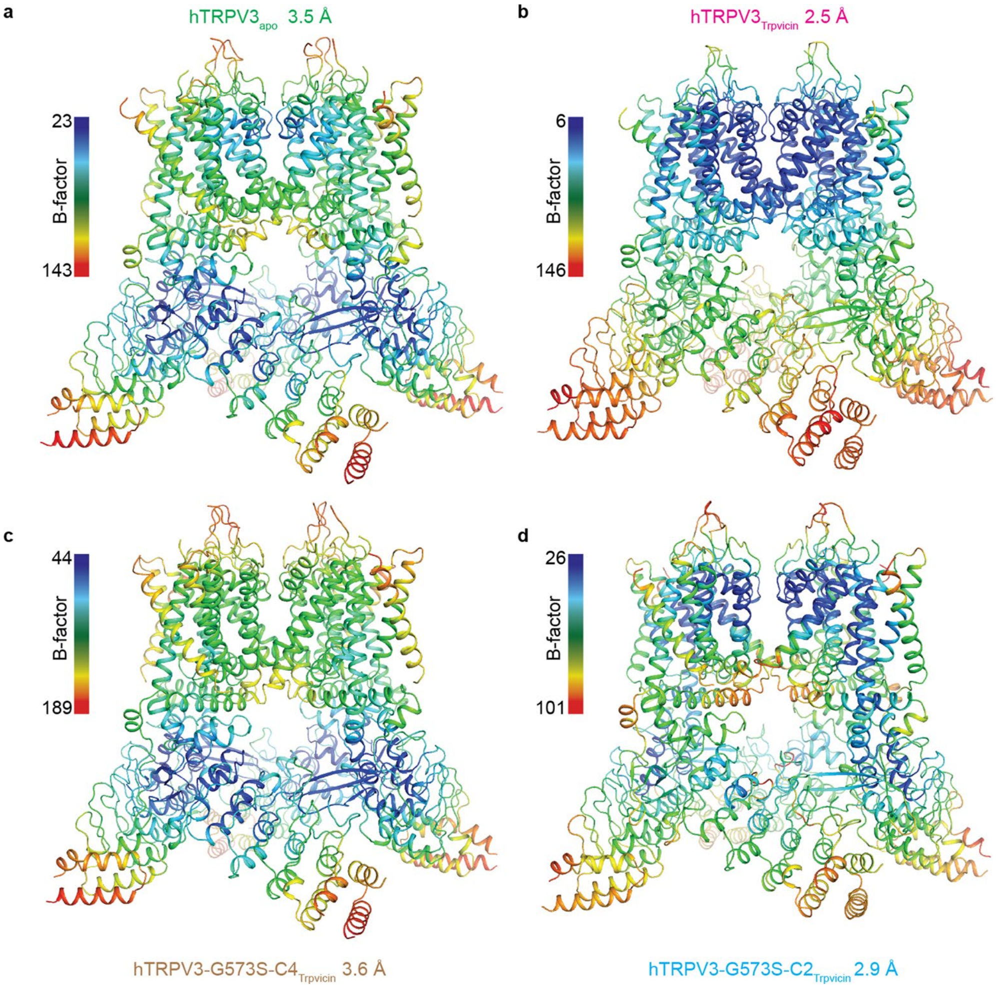

Extended Data Fig. 4 | B-factor distribution in hTRPV3 structures. a-d, The Cα B-factors are depicted on the refined structure from dark blue (lowest B-factor) to red (highest B-factor) for hTRPV3$_{apo}$ (**a**), hTRPV3$_{Trpvicin}$ (**b**), hTRPV3-G573S-C4$_{Trpvicin}$ (**c**) and hTRPV3-G573S-C2$_{Trpvicin}$ (**d**) respectively.

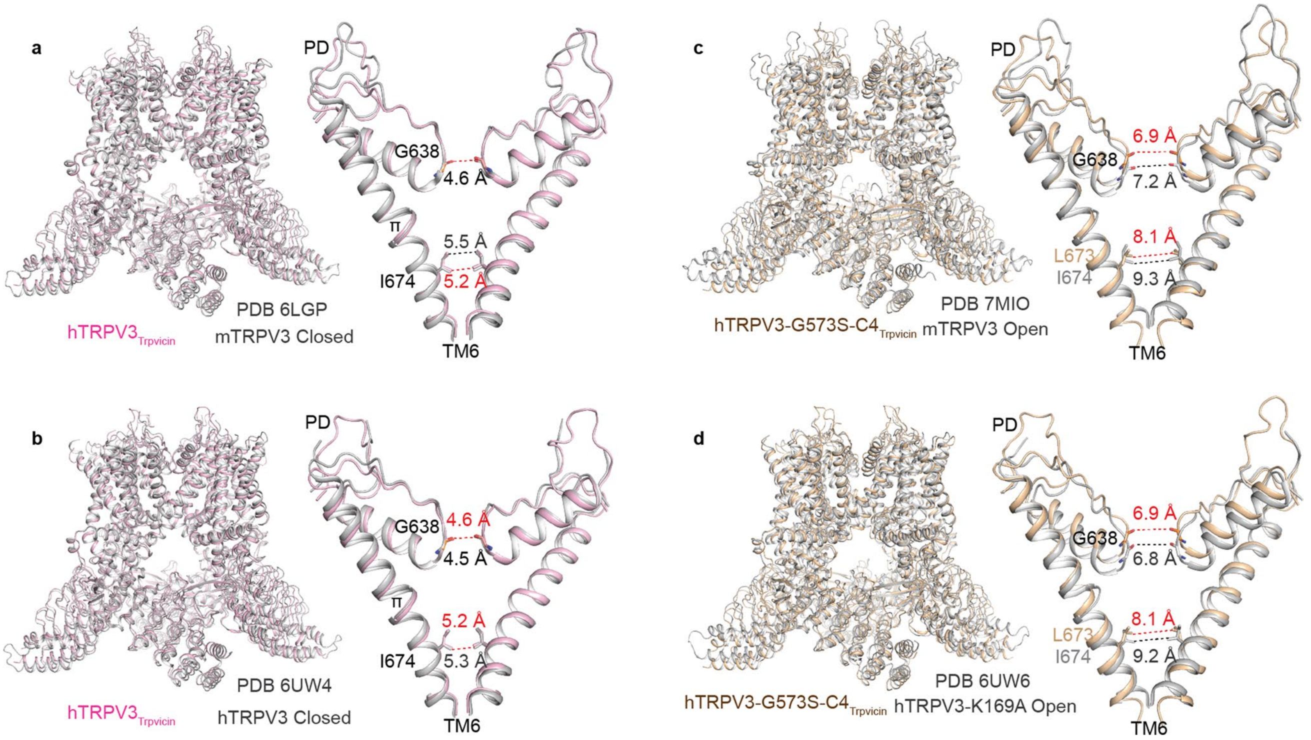

Extended Data Fig. 5 | Structural comparison of TRPV3 structures determined in open and closed states. **a**,**b**, Superposition of hTRPV3$_{\mathrm{Trpvicin}}$ (light pink) with mouse TRPV3 structure (PDB code: 6LGP, grey, (**a**)) and human TRPV3 structure (PDB code: 6UW4, grey, (**b**)) at closed states viewed parallel to the membrane. **c**,**d**, Superposition of hTRPV3-G573S-C4$_{\mathrm{Trpvicin}}$ (wheat) with mouse TRPV3 structure (PDB code: 7MIO, grey, (**c**)) and human TRPV3-K169A structure (PDB code: 6UW6, grey, (**d**)) at open states viewed parallel to the membrane. On the right, showing the close-up views for the comparisons of S6 and pore-helices.

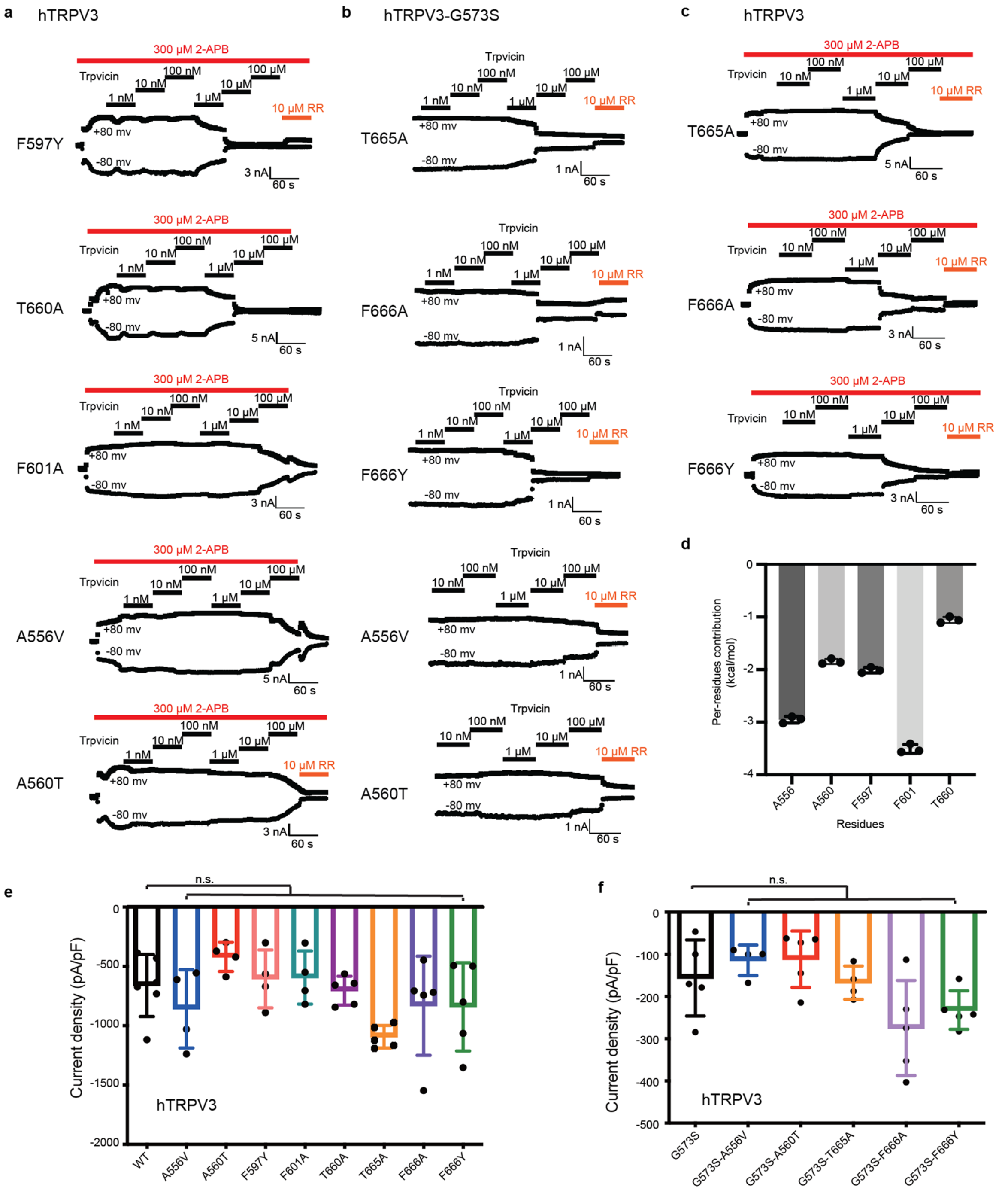

Extended Data Fig. 6 | The binding sites function evaluation. a, The representative current traces of hTRPV3 mutants in the VSLD-PD binding sites in response to 2-APB (300 μM, red bar) and co-application of increasing concentrations of Trpvicin (from 1 nM to 100 μM, black bar), at ±80 mV. **b**, The representative current traces of hTRPV3-G573S mutants in the pore binding sites and the VSLD-PD binding sites inhibited by increasing concentrations of Trpvicin at ±80 mV. 10 μM RR was used to assess the whole amplitudes of leak currents. **c**, The representative current traces of hTRPV3 mutants in the pore binding sites in response to 2-APB and co-application of increasing concentrations of Trpvicin at ±80 mV. **d**, Per-residues binding energy calculated by MM-GBSA. Data are presented as mean values +/− SD of triplicates. **e**, The hTRPV3 mutants function similarly to the hTRPV3-WT in response to 300 μM 2-APB. The current density at −80 mV of hTRPV3 mutant channels activated by 300 μM 2-APB, compared with hTRPV3-WT. One-way ANOVA followed by Bonferroni post-tests (WT, *n* = 6; A556V, *n* = 4; A560T, *n* = 4; F597Y, *n* = 4; F601A, *n* = 4; T660A, *n* = 5; T665A, *n* = 5; F666A, *n* = 5; F666Y, *n* = 5). Data are presented as mean values + /- SEM. WT, wild type. **f**, The double mutation variants function similarly to the hTRPV3-G573S. The current density of leak currents at −80 mV of hTRPV3 double mutation variants, compared with hTRPV3-G573S. One-way ANOVA followed by Bonferroni post-tests (hTRPV3-G573S, *n* = 5; G573S-A556V, *n* = 4, G573S-A560T, *n* = 4; G573S-T665A, *n* = 4; G573S-F666A, *n* = 5; G573S-F666Y, *n* = 4). Data are presented as mean values + /- SEM; n.s., not significant.

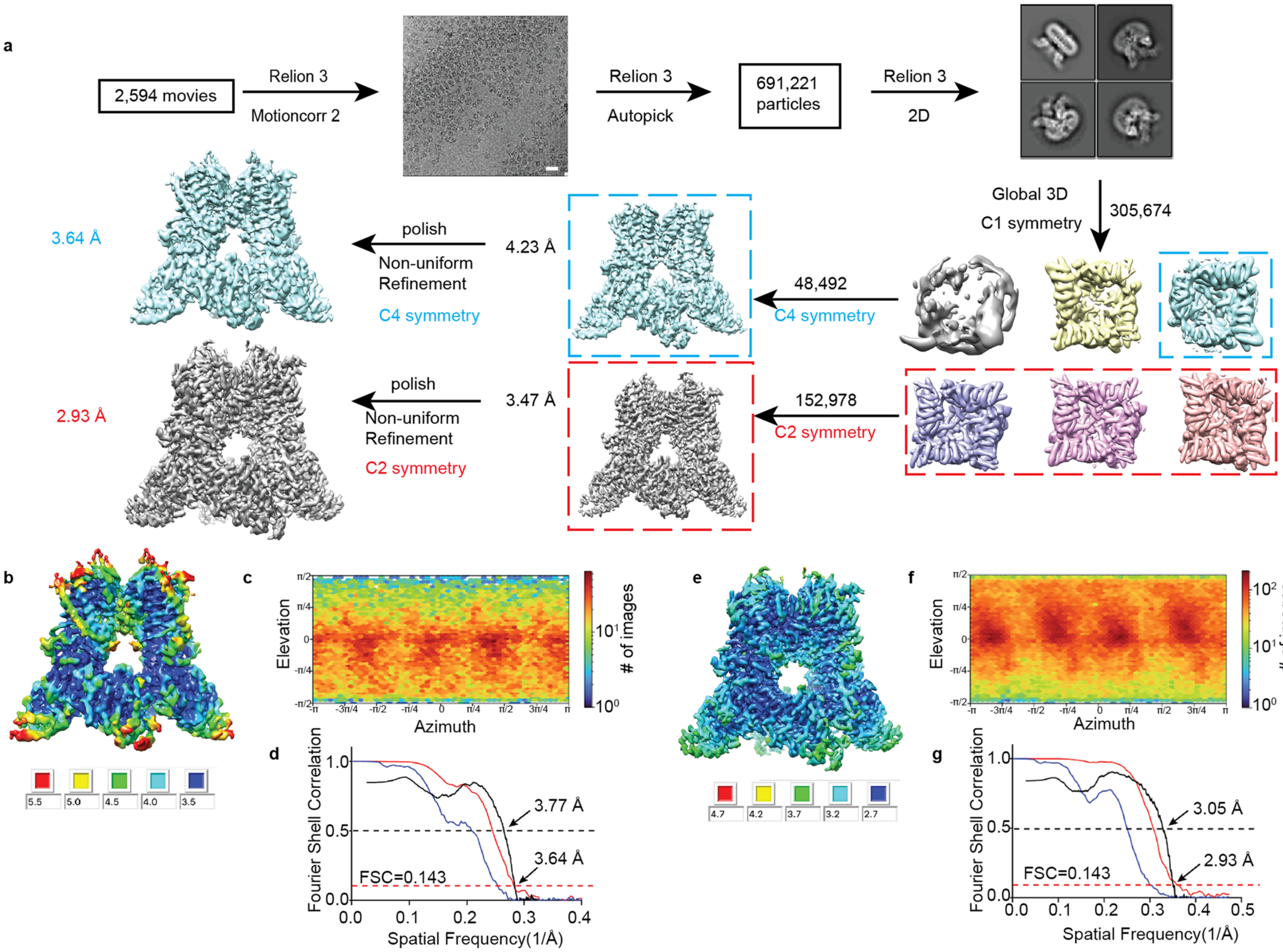

Extended Data Fig. 7 | Cryo-EM data processing of hTRPV3-G573S. a, Flow chart of cryo-EM data processing. A total of 691,221 particles were picked from 2,594 micrographs. A representative motion-corrected micrograph of the dataset is shown here (Bar = 400 Å). Several rounds of 2D and 3D classifications were conducted to clean particles, followed by Bayesian Polish and CTF Refine to improve image quality. The final map was refined at 3.64 Å and 2.93 Å for hTRPV3-G573S-C4 and hTRPV3-G573S-C2 according to the GSFSC criterion, respectively. (**b** & **e**) Local resolution distribution of the sharpened map of the hTRPV3-G573S-C4$_{\text{Trpvicin}}$ and hTRPV3-G573S-C2$_{\text{Trpvicin}}$. (**c** & **f**) Particle angular distribution calculated in cryoSPARC for the final reconstruction of hTRPV3-G573S-C4$_{\text{Trpvicin}}$ and hTRPV3-G573S-C2$_{\text{Trpvicin}}$. (**d** & **g**) Fourier Shell Correlations (FSC) of the final map of the hTRPV3-G573S-C4$_{\text{Trpvicin}}$ and hTRPV3-G573S-C2$_{\text{Trpvicin}}$, calculated between two independently refined half-maps before (blue) and after (red) post-processing, overlaid with an FSC curve calculated between the cryo-EM density map and the structural model shown in black.

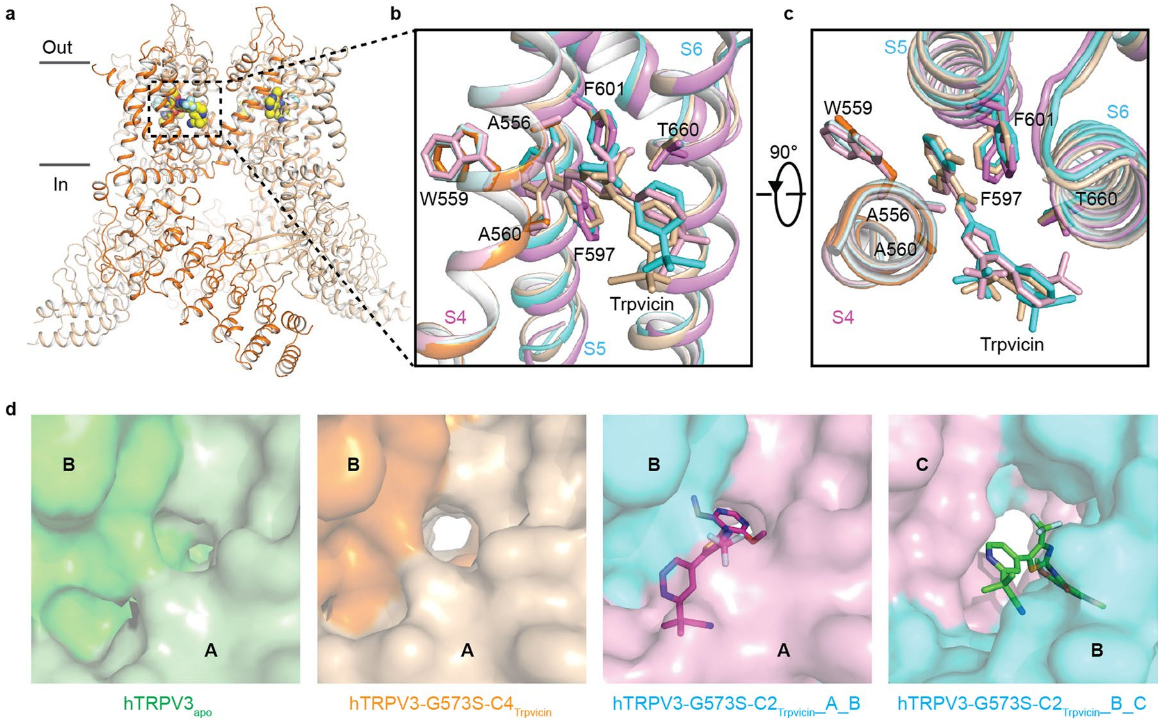

hTRPV3$_{\text{apo}}$ hTRPV3-G573S-C4$_{\text{Trpvicin}}$ hTRPV3-G573S-C2$_{\text{Trpvicin}}$_A_B hTRPV3-G573S-C2$_{\text{Trpvicin}}$_B_C

Extended Data Fig. 8 | Comparison of the Trpvicin VSLD-PD site and fenestrations of hTRPV3$_{\text{Trpvicin}}$, G573S-C4$_{\text{Trpvicin}}$, and G573S-C2$_{\text{Trpvicin}}$. **a**, Side view of hTRPV3-G573S-C4 in complex with Trpvicin colored in yellow and wheat. The Trpvicin is shown in spheres. **b**-**c**, Close-up views for the comparison of the Trpvicin VSLD-PD binding site in G573S-C4$_{\text{Trpvicin}}$ (wheat), hTRPV3$_{\text{Trpvicin}}$ (light pink), and G573S-C2$_{\text{Trpvicin}}$ (cyan). The Trpvicin is shown in sticks. **d**, Side-views of fenestrations formed by two adjacent pore domains from hTRPV3$_{\text{apo}}$, hTRPV3-G573S-C4$_{\text{Trpvicin}}$, hTRPV3-G573S-C2$_{\text{Trpvicin}}$-chainA/chainB, and hTRPV3-G573S-C2$_{\text{Trpvicin}}$-chainB/chainC, respectively.

https://doi.org/10.1038/s41589-022-01166-5

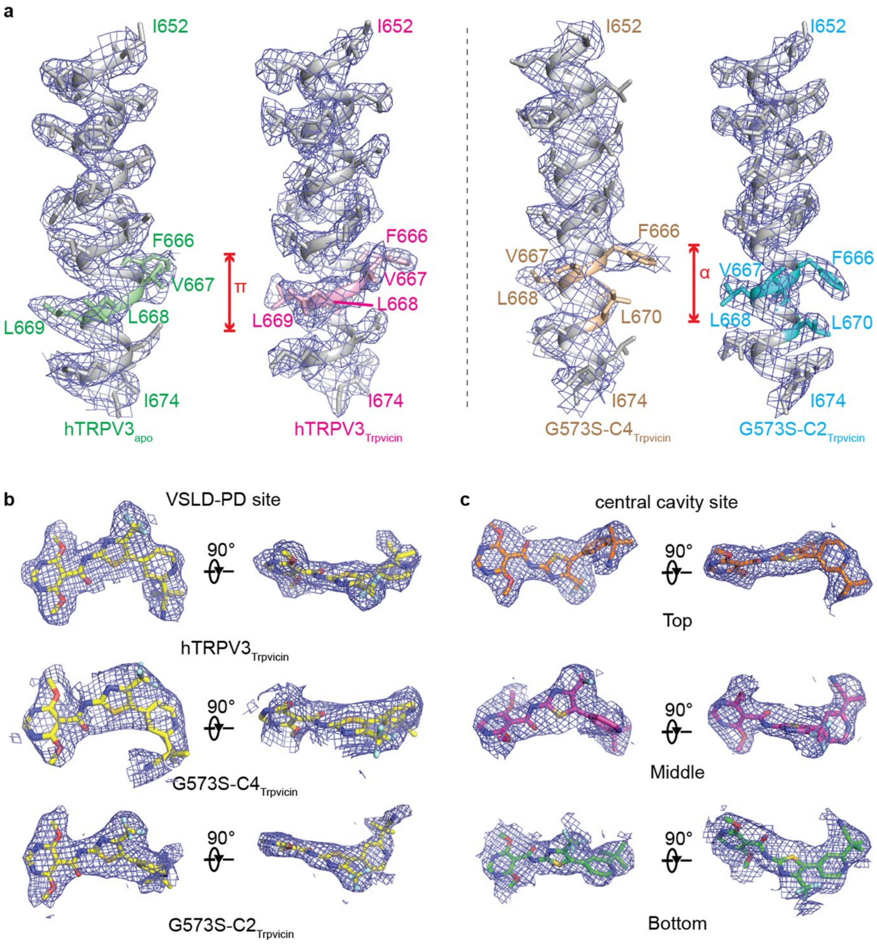

Extended Data Fig. 9 | Representative cryo-EM density of S6 helix and Trpvicin. **a**, Cryo-EM density for S6 helix of hTRPV3$_{apo}$, hTRPV3$_{Trpvicin}$, hTRPV3-G573S-C4$_{Trpvicin}$, and hTRPV3-G573S-C2$_{Trpvicin}$. The π- and α-helix on S6 helices are highlighted and related resides are labeled accordingly. **b**, Cryo-EM density for Trpvicin bound to hTRPV3$_{Trpvicin}$, hTRPV3-G573S-C4$_{Trpvicin}$, and hTRPV3-G573S-C2$_{Trpvicin}$ at the VSLD-PD site. **c**, Cryo-EM density for Trpvicin bound to the central cavity of hTRPV3-G573S-C2$_{Trpvicin}$.

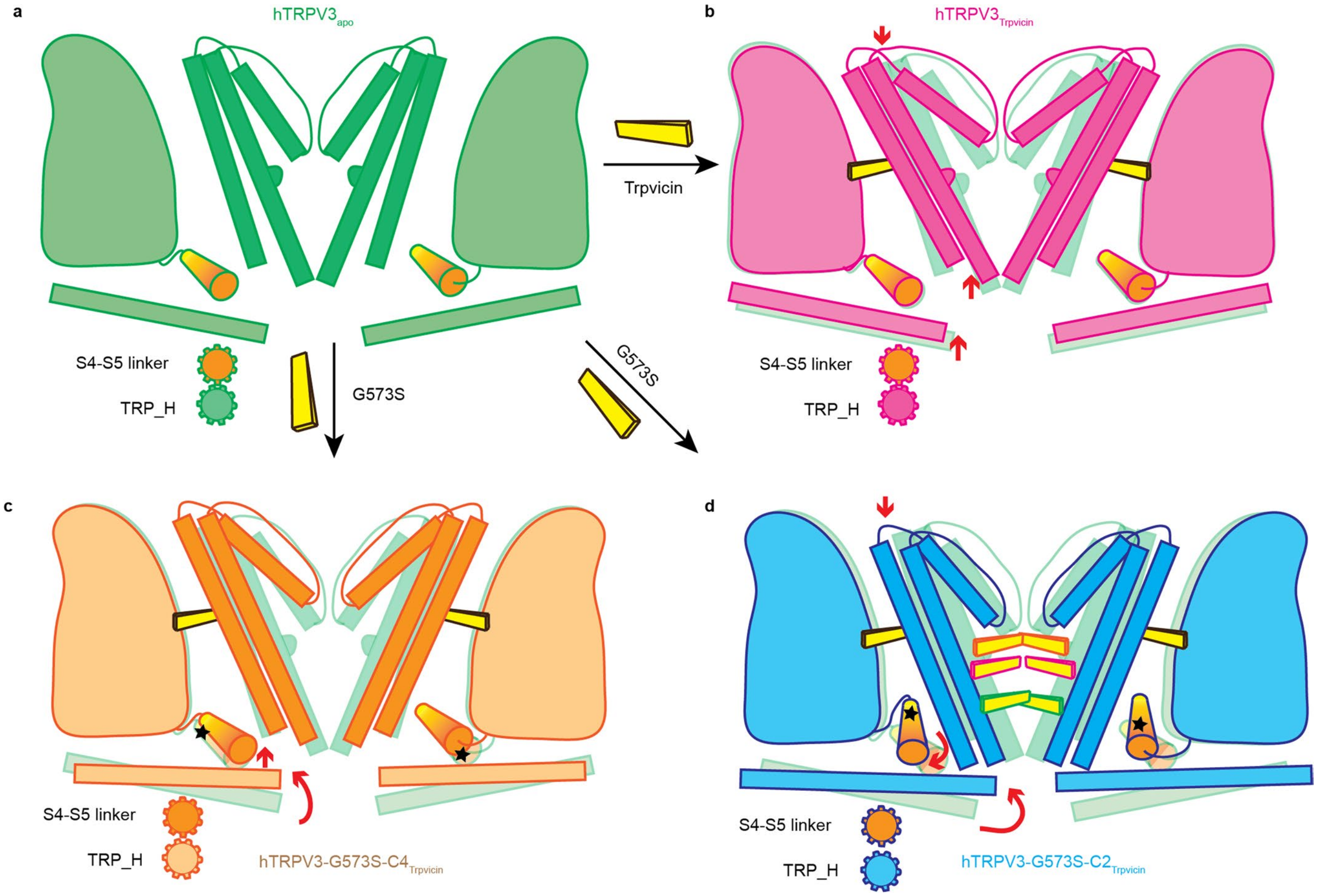

Extended Data Fig. 10 | A cartoon model for the antagonist inhibition mechanism of TRPV3 and G573S mutant. a, The hTRPV3$_{apo}$ at closed-state. The hTRPV3$_{apo}$ VSLD domain, linker region, and TRP helix from the two opposing subunits and the ion-conduction pores from the adjacent subunit are shown. **b**, Conformational changes induced by the Trpvicin bound to TRPV3. The Trpvicin wedges into the VSLD-PD site between the VSLD and the PD from the adjacent subunit, inducing conformational changes of the entire channel into a more closed state. The movements of individual domains are indicated by arrows. **c**, Conformational changes induced by G573S mutation expand the ion path at both the SF and the activation gate in the C4 symmetry. **d**, Trpvicin molecules enter the central cavity of the G573S mutant channel, inducing structural rearrangements to form C2 symmetry and block ion permeation. The pore-lining S6 helices undergo π- to α-helix transitions for the G573S structures. Two gear shapes stand for the interaction between the S4-S5 linker and TRP helix. In the hTRPV3$_{Trpvicin}$ structure, the S4-S5 linker and TRP helix interaction was strengthened compared to hTRPV3$_{Apo}$ because of the shrinking caused by Trpvicin binding while in the G573S mutant, the interaction was interrupted, showing loosely interaction in hTRPV3-G573S-C4$_{Trpvicin}$ structure and even less in hTRPV3-G573S-C2$_{Trpvicin}$ structure because of the twisting between the two domains. The G573S mutation position is indicated by a black asterisk.

nature research

Corresponding author(s): Xiaoguang Lei, Yong Yang, Daohua Jiang

Last updated by author(s): Aug 26, 2022

Reporting Summary

Nature Research wishes to improve the reproducibility of the work that we publish. This form provides structure for consistency and transparency in reporting. For further information on Nature Research policies, see our Editorial Policies and the Editorial Policy Checklist.

Statistics

For all statistical analyses, confirm that the following items are present in the figure legend, table legend, main text, or Methods section.

n/a	Confirmed	
☐	☒	The exact sample size (*n*) for each experimental group/condition, given as a discrete number and unit of measurement
☐	☒	A statement on whether measurements were taken from distinct samples or whether the same sample was measured repeatedly
☐	☒	The statistical test(s) used AND whether they are one- or two-sided *Only common tests should be described solely by name; describe more complex techniques in the Methods section.*
☒	☐	A description of all covariates tested
☐	☒	A description of any assumptions or corrections, such as tests of normality and adjustment for multiple comparisons
☐	☒	A full description of the statistical parameters including central tendency (e.g. means) or other basic estimates (e.g. regression coefficient) AND variation (e.g. standard deviation) or associated estimates of uncertainty (e.g. confidence intervals)
☐	☒	For null hypothesis testing, the test statistic (e.g. *F*, *t*, *r*) with confidence intervals, effect sizes, degrees of freedom and *P* value noted *Give P values as exact values whenever suitable.*
☒	☐	For Bayesian analysis, information on the choice of priors and Markov chain Monte Carlo settings
☒	☐	For hierarchical and complex designs, identification of the appropriate level for tests and full reporting of outcomes
☒	☐	Estimates of effect sizes (e.g. Cohen's *d*, Pearson's *r*), indicating how they were calculated

Our web collection on statistics for biologists contains articles on many of the points above.

Software and code

Policy information about availability of computer code

Data collection	SerialEM 3.8 was used for cryo-EM image collection; PatchMaster (v2x69) software (HEKA Instruments) and EPC10 amplifier was used for electrophysiological data collection
Data analysis	MotionCor 2 1.3.2, GCTF 1.06, cryoSPARC 3.0, RELION 3.1, UCSF-Chimera v1.14, PyMOL 2.5.2, ChimeraX 1.11, COOT 0.8.9.2, PHENIX 1.16, GraphPad Prism 8.4.0, Igor Pro 6.3.7.2, PKsolver2.0, ChemDraw 20.1, ImageJ 1.52i, Adobe Illustrator CS6, AmberTools21; Amber20

For manuscripts utilizing custom algorithms or software that are central to the research but not yet described in published literature, software must be made available to editors and reviewers. We strongly encourage code deposition in a community repository (e.g. GitHub). See the Nature Research guidelines for submitting code & software for further information.

Data

Policy information about availability of data

All manuscripts must include a data availability statement. This statement should provide the following information, where applicable:

- Accession codes, unique identifiers, or web links for publicly available datasets
- A list of figures that have associated raw data
- A description of any restrictions on data availability

The NCBI Reference Sequence of proteins is provided in Methods Plasmid constructs part.
The novel structures determined in this study are deposited in PDB Bank and Electron Microscopy Data Bank (EMDB):
hTRPV3: 7XJ3 [http://doi.org/10.2210/pdb7XJ3/pdb]; EMD-33218 [https://www.emdataresource.org/EMD-33218]
hTRPV3-Trpvicin: 7XJ0 [http://doi.org/10.2210/pdb7XJ0/pdb]; EMD-33214 [https://www.emdataresource.org/EMD-33214]
hTRPV3-G573S-Trpvicin-C4: 7XJ1 [http://doi.org/10.2210/pdb7XJ1/pdb]; EMD-33216 [https://www.emdataresource.org/EMD-33216]

hTRPV3-G573S-Trpvicin-C2: 7XJ2 [http://doi.org/10.2210/pdb7XJ2/pdb]; EMD-33217 [https://www.emdataresource.org/EMD-33217]
Publicly available data set used in this study is: 6mho

Field-specific reporting

Please select the one below that is the best fit for your research. If you are not sure, read the appropriate sections before making your selection.

☒ Life sciences ☐ Behavioural & social sciences ☐ Ecological, evolutionary & environmental sciences

For a reference copy of the document with all sections, see nature.com/documents/nr-reporting-summary-flat.pdf

Life sciences study design

All studies must disclose on these points even when the disclosure is negative.

Sample size	No statistical methods used to predetermine sample size. For the cryo-EM studies, the number of micrographs is determined by the available microscope time. For all binding experiment, inhibition assays and animal experiments were performed in triplicate or more, which were sufficient to support the conclusions. Samples sizes are indicated in the respective Methods and figure legends. Data were analyzed by fitting various ligand concentrations and readouts using appropriate equations in GraphPad Prism 8.4.0.
Data exclusions	No data was excluded.
Replication	Each experiments were replicated at least 3 times and described in the manuscript . All attempts at replication were successful.
Randomization	For animal experiments, mice were always randomly assigned into different groups. For the rest studies, randomization was not relevant, as the independent variables were sufficient for the interpretation with in this study.
Blinding	For animal experiments, the investigators were blinded to group allocation during both data collection and analysis. For cryo-EM structure determination and other functional studies, blinding is not necessary due to the nature of these experiments do not requires subject assessment of the data that may influence the validity of the results.

Reporting for specific materials, systems and methods

We require information from authors about some types of materials, experimental systems and methods used in many studies. Here, indicate whether each material, system or method listed is relevant to your study. If you are not sure if a list item applies to your research, read the appropriate section before selecting a response.

Materials & experimental systems

n/a	Involved in the study	
☒	☐	Antibodies
☐	☒	Eukaryotic cell lines
☒	☐	Palaeontology and archaeology
☐	☒	Animals and other organisms
☒	☐	Human research participants
☒	☐	Clinical data
☒	☐	Dual use research of concern

Methods

n/a	Involved in the study	
☒	☐	ChIP-seq
☒	☐	Flow cytometry
☒	☐	MRI-based neuroimaging

Eukaryotic cell lines

Policy information about cell lines

Cell line source(s)	Sf9 insect cells (Invitrogen, USA), HEK293F GnTI– (Gibco, USA), HEK 293-T cells (Gibco, USA)
Authentication	Cell lines were not authenticated.
Mycoplasma contamination	All cell lines were negative for mycoplasma contamination.
Commonly misidentified lines (See ICLAC register)	Commonly misidentified lines were not used in this study.

Animals and other organisms

Policy information about studies involving animals; ARRIVE guidelines recommended for reporting animal research

Laboratory animals	The study involved mouse strain CD-1 male at the age of 8 weeks and mouse strain C57BL/6J male at the age of 8-12 weeks, together with both female and male Trpv3 knock-in mice at the age of 7-13 weeks.
Wild animals	The study did not involve wild animals.
Field-collected samples	The study did not involve samples collected from the field.
Ethics oversight	All mouse experiments were approved by the Institutional Animal Care and Use Committees of Peking University First Hospital (Beijing, China).

Note that full information on the approval of the study protocol must also be provided in the manuscript.